J. Fluid Mech. (1998), *vol.* 356, *pp.* 93–124. Printed in the United Kingdom

Theory and experiment on the low-Reynolds-number expansion and contraction of a bubble pinned at a submerged tube tip

By HARRIS WONG†, DAVID RUMSCHITZKI AND CHARLES MALDARELLI

The Levich Institute and Chemical Engineering Department, The City College of CUNY

(Received 8 December 1995 and in revised form 11 September 1997)

The expansion and contraction of a bubble pinned at a submerged tube tip and driven by constant gas flow rate Q are studied both theoretically and experimentally for Reynolds number $Re \ll 1$. Bubble shape, gas pressure, surface velocities, and extrapolated detached bubble volume are determined by a boundary integral method for various Bond ($Bo = \rho g a^2/\sigma$) and capillary ($Ca = \mu Q/\sigma a^2$) numbers, where a is the capillary radius, ρ and μ are the liquid density and viscosity, σ is the surface tension, and g is the gravitational acceleration.

Bubble expansion from a flat interface to near detachment is simulated for a full range of Ca (0.01–100) and Bo (0.01–0.5). The maximum gas pressure is found to vary almost linearly with Ca for $0.01 \leqslant Ca \leqslant 100$. This correlation allows the maximum bubble pressure method for measuring dynamic surface tension to be extended to viscous liquids. Simulated detached bubble volumes approach static values for $Ca \ll 1$, and asymptote as $Q^{3/4}$ for $Ca \gg 1$, in agreement with analytic predictions. In the limit $Ca \to 0$, two singular time domains are identified near the beginning and the end of bubble growth during which viscous and capillary forces become comparable.

Expansion and contraction experiments were conducted using a viscous silicone oil. Digitized video images of deforming bubbles compare well with numerical solutions. It is observed that a bubble contracting at high Ca snaps off.

1. Introduction

The growth and detachment of a submerged bubble from either a tube tip or an orifice represent a fundamental process in many branches of science. The noise created by bubbles detaching from an underwater nozzle is of interest in acoustics and has been studied theoretically and experimentally by Longuet-Higgins, Kerman & Lunde (1991). A surfactant-laden bubble expanding or contracting at a tube tip has been used for measuring dynamic surface tension (Edwards, Brenner & Wasan 1993; Miller, Joos & Faineman 1994). When bubbles are generated from a submerged orifice at a constant flow rate, the intervals between successive bubbles are found to be chaotic at high Re, and the experimental set-up has been suggested as a simple tool for studying chaos (Tritton & Egdell 1993).

The size of detached bubbles has been studied extensively owing to its importance in direct-contact heat and mass transfer operations in chemical, metallurgical, and

† Permanent address: Mechanical Engineering Department, Louisiana State University, Baton Rouge, LA 70803-6413, USA.

biomedical systems (Kumar & Kuloor 1970; Clift, Grace & Weber 1978; Tsuge & Hibino 1983). At low gas-flow rates, a bubble grows quasi-statically and takes on roughly the static pendant shape, which results from a local balance of capillary and hydrostatic pressures. When the bubble volume grows beyond a maximum value V_{max}, the buoyancy force exceeds the anchoring surface tension force, and the bubble pinches off (see, for example, Longuet-Higgins *et al.* 1991). This complex dynamics and evolution of the pinching process is ignored by the quasi-static models, which take the detached volume (V_d) to be the volume above the neck of the static bubble when the bubble volume $V = V_{max}$:

$$V_d = \frac{2\pi}{Bo}\Psi(Bo), \tag{1.1}$$

where V, V_{max}, and V_d are made dimensionless by a^3. The function $\Psi(Bo)$ depends weakly on Bo and is always less than one. Experiments at slow flow rates have shown that the detached volume is usually predicted by the upper bound $2\pi/Bo$ within a factor of two (Datta, Napier & Newitt 1950; Van Krevelen & Hoftijzer 1950; Bhavaraju, Russell & Blanch 1978).

At high flow rates, viscous and inertial forces distort an emerging bubble from the static shape. These forces oppose the buoyancy force and delay bubble detachment. The effects of the inertia forces have been the focus of most theoretical and experimental studies because the Reynolds number ($Re = \rho Q/a\mu$) is usually high for bubble formation in interphase contacting equipment. The equipment uses water and sieve plates with orifice radii in the range from 0.01 to 0.5 cm. Even for flow rates as low as 0.05 $cm^3\ s^{-1}$, the Reynolds number is 10 for the larger orifices. To maintain sufficient heat or mass transfer, the flow rates are usually larger ($Q > 10^2\ cm^3\ s^{-1}$). Thus, the inertial forces dominate the viscous forces under operation conditions in water. This has motivated a series of inviscid modelling studies with accompanying water experiments that have thoroughly investigated the inertial regime.

1.1. *Inviscid models*

Davidson & Schuler (1960*a*) first developed an inviscid model for the growth of a bubble from a hole in the top plate of a submerged gas chamber. The model assumes that the bubble grows spherically from a point source, and that the bubble bottom dips below the top plate. As the bubble grows, the buoyancy force increases and the bubble accelerates upward. An integral force balance in the vertical direction equates the acceleration of the added mass of the liquid, $\rho V c_A$ (with the added mass coefficient $c_A = 11/16$ for a gas sphere moving normally to a wall), to buoyancy:

$$We\frac{\mathrm{d}}{\mathrm{d}t}\left(Vc_A\frac{\mathrm{d}z_0}{\mathrm{d}t}\right) = Bo\,V, \tag{1.2}$$

where $z_0(t)$ is the height (made dimensionless by a) of the bubble centre above the orifice, t is time scaled by a^3/Q, and We is the Weber number ($We = \rho Q^2/\sigma a^3$). Flow rates are assumed large enough so that the surface tension force tethering the bubble is negligible for all but the earliest times. Davidson & Schuler (1960*a*) distinguished regimes of constant flow rate and constant gas pressure. For constant flow rate the above equation can be integrated directly. For constant pressure the gas pressure drop across the orifice is predicted using an orifice equation to yield the gas flow rate and hence the bubble radius as a function of time. LaNauze & Harris (1972, 1974) improved this model to account for the radial liquid acceleration and the gas

momentum. Walters & Davidson (1963) extended the model to bubbles growing at a tube tip. They used (1.2) and an orifice equation with $c_A = \frac{1}{2}$, the value for a bubble translating in an infinite medium.

In these spherical models, the bubble is taken as detached when its bottom point is at the same level as the orifice (point source). With this criterion and with constant flow rate (i.e. $V = t$), (1.2) can be directly integrated up to 'detachment':

$$V_d = \left[\frac{3(4c_A)^3}{4\pi}\right]^{1/5} \left(\frac{We}{Bo}\right)^{3/5}. \tag{1.3}$$

(Note that $We/Bo = Q^2/ga^5$ is independent of surface tension.) Similar though not analytic expressions are obtained for the constant pressure case. Comparison of the results of this model with experiments by Davidson & Schuler (1960*a*) and LaNauze & Harris (1974) shows good agreement for the constant flow rate case, but less consistent agreement for the constant pressure case.

The more sophisticated models of bubble detachment also assume that the growing bubble is spherical, but the bubble is not allowed to dip below the top plate. The motion of the bubble is divided into two stages: expansion and lift-off (Kupferberg & Jameson 1969; Wraith 1971; Ramakrishnan, Kumar & Kuloor 1969; Satyanarayan, Kumar & Kuloor 1969; Khurana & Kumar 1969; Tsuge & Hibino 1983). In the expansion stage, the spherical bubble is small and remains in contact with the plate at a point, because the buoyancy force is weak compared with the surface tension and inertia forces. Lift-off commences when these forces balance exactly, and this defines a critical volume. After lift-off the spherical bubble is connected to the plate by a gas thread that feeds the bubble growth. The bubble is taken as detached when the gas thread reaches a specific length. Depending on the particular model, the final thread length ranges from the orifice diameter to the sum of the bubble radius at lift-off plus the orifice radius.

While the two-stage models are computationally efficient and can be used to fit detached-volume data, they lack physical insight into the detachment mechanisms. Marmur & Rubin (1976) (and later Tan & Harris 1986 and Liow & Gray 1988) constructed a non-spherical model by discretizing the interface into a series of mass elements. At each element, the hydrostatic and capillary pressures balance the inertia of the added mass of the liquid. The bubble is assumed pinned at an orifice. Simulations depict qualitatively though crudely the bubble shape and neck formation preceding detachment. Detached volumes are obtained by integrating the equations until the interfaces touch at the neck. The results agree well with experimental data, indicating that when the necking process is described there is no need for arbitrary lift-off and detachment criteria.

A numerically exact treatment of the interface shape is Oguz & Prosperetti's (1993) boundary integral solution of the inviscid flow field. They analysed the growth of a bubble from a submerged needle. The gas flow through the needle is supplied by a constant pressure reservoir, and obeys a Hagen–Poiseuille law. Rather than pinning the bubble to the needle tip, the contact line moves so as to prevent the contact angle from becoming smaller than 90°. The computed detached volume V_d agrees with the quasi-static prediction (1.1) at low flow rates. As Q becomes large, V_d asymptotically increases with $Q^{6/5}$ as given by (1.3). This change in behaviour occurs over one decade in the characteristic flow rate. Oguz & Prosperetti (1993) also compared their calculated bubble shapes with the experimental results of Longuet-Higgins *et al.* (1991) and obtained qualitative agreement.

1.2. *Viscous models*

Clearly the regime of $Re \gg 1$ has been completely studied. This paper studies the less well understood case of $Re \ll 1$. This viscous regime was the focus of Davidson & Schuler's (1960*b*) single stage spherical model. In that model, surface tension is again neglected, and buoyancy balances the Stokes drag in the vertical direction. They show that for a constant flow rate the detached volume varies with $Q^{3/4}$, rather than with $Q^{6/5}$ for inviscid flow. This dependence is in good agreement with their own experimental results. Two-stage inertial models have also included the effects of viscosity by adding a viscous drag term to (1.1) in the lift-off stage and to the balance of forces in the expansion stage (Ramakrishnan *et al.* 1969; Tsuge & Hibino 1983).

This paper studies the viscous regime with surface tension. Bubble shape and liquid flow are calculated using a boundary integral method. We also perform experiments in a viscous silicone oil that ensures high capillary and low Reynolds numbers. The calculated shapes agree quantitatively with the measured ones during both expansion and contraction.

As already mentioned, the viscous regime is not usually applicable to conditions for bubble contacting in water. However, for bubble contacting in more viscous fluids such as polymer melts, molten metals, and molten glass, the Reynolds number can be smaller than one under operating conditions (Prosperetti, Oguz & Won 1997). Thus, one of the purposes of this study is to calculate the detached bubble volume over a wide range of Ca and Bo. A second objective is to describe the liquid motion, particularly the interfacial convection, for better understanding of surfactant transport, as detailed below.

1.3. *Methods for measuring dynamic surface tension*

A class of methods of measuring dynamic surface tension uses bubbles expanding from a capillary tip into a surfactant solution. These methods include the maximum bubble pressure method and the pendant bubble method (Miller *et al.* 1994). In the maximum bubble pressure method, bubbles are formed continuously at the tip of a needle, and the gas pressure is measured relative to the liquid pressure. Typically, the bubble motion is dominated by surface tension with $Ca \ll 1$, $Bo \ll 1$, and $We \ll 1$. After a bubble detaches, a new bubble emerges with a rather flat interface, so the gas pressure is close to zero. As the new bubble grows into a hemisphere, the bubble radius reaches minimum; the radius of the hemisphere equals the tube radius a. At this instant, the gas pressure attains a maximum value of $2\sigma/a$, as determined by the Young–Laplace equation. The surface tension σ is then calculated from this equation using the measured maximum gas pressure and the tube radius a. This is the surface tension when the bubble is hemispherical, which occurs at a particular surface age, with the age of a freshly created bubble taken as zero. At a higher gas flow rate, a new bubble reaches the hemispherical shape faster, and the surface age of the hemispherical bubble decreases. Thus, by varying the gas flow rate, the surface tension at different surface ages is determined.

In the pendant bubble method, a bubble is formed at the tip of a needle and grows to a pendant shape under the action of gravity ($Bo \sim 1$) before the growth is terminated. Surfactant molecules adsorb onto the bubble surface until they reach equilibrium. This equilibrium surfactant concentration is then perturbed by expanding or contracting the bubble at $Ca \ll 1$ and $We \ll 1$. Under these conditions, the bubble shape resembles that of the static bubble and obeys the Young–Laplace equation. The surface tension at each instant is obtained by comparing the digitized bubble image with the static bubble shape predicted by the Young–Laplace equation (Miller *et al.*

1993*a*, *b*; Pan, Green & Maldarelli 1995). This again yields the surface tension at different surface ages. In both methods, the dynamic tension yields the surface surfactant concentration as a function of time using the surfactant equation of state. Once the dynamic adsorption is measured, mathematical models of surfactant transport must be solved and compared to the experimental profiles to determine surfactant transport parameters such as the diffusion and the kinetic exchange coefficients. Correct modelling involves an adequate description of the flow field, particularly the surface convection. To date similar modelling has only accounted for radial flow (Joos & Rillaerts 1981; MacLeod & Radke 1994). The computed velocity field developed here will provide a more complete picture of how surfactant is convected at the low end of the range of Reynolds numbers used for both the maximum bubble pressure and pendant bubble methods.

The maximum bubble pressure method is usually applicable only for bubbles expanding at $Bo \ll 1$ and $Ca \ll 1$. Here, a simple empirical relation is found for the maximum bubble pressure that allows the maximum bubble pressure method to be extended to $Bo \sim 1$ and $Ca \gg 1$. Thus, the method can be applied to measure dynamic tensions for large bubbles and for liquids more viscous than water.

This paper is organized as follows. The mathematical model and the governing equations are presented in §2. The boundary integral equations are formulated in §3. These equations are solved by the Nystrom method in §4. Numerical results for bubble expansion from a planar interface are presented in §5. Bubble shapes for contractions from a static pendant configuration are presented in §6. Section 7 describes the experimental set-up, procedures, and results, and the quantitative comparison with numerical simulations. The conclusions are in §8.

2. Mathematical model

Figure 1 shows the physical situation. A static, clean bubble sits at the tip of a semi-infinite tube of radius a and is surrounded by a surfactant-free, Newtonian liquid of viscosity μ and density ρ. At time $t = 0$, the bubble is either expanded or contracted at a constant volume flow rate Q. The resulting liquid flow is in the creeping flow regime and obeys the Stokes equations, which in dimensionless form read,

$$\boldsymbol{\nabla} \cdot \boldsymbol{T} = -\boldsymbol{\nabla} p + Ca \nabla^2 \boldsymbol{u} - Bo\, \boldsymbol{e}_z = 0, \tag{2.1a}$$

$$\boldsymbol{\nabla} \cdot \boldsymbol{u} = 0, \tag{2.1b}$$

where $\boldsymbol{T}$ is the stress tensor with the gravity force incorporated, $\boldsymbol{u}$ is the velocity, p is the pressure relative to $p(r \to \infty, z = 0)$, $\boldsymbol{\nabla}$ is the gradient operator, and $\boldsymbol{e}_z$ is an upward-pointing unit vector. A set of cylindrical coordinates (r, z) is defined with origin at the tube tip (figure 1). The capillary number $Ca \equiv \mu Q / a^2 \sigma$ and the Bond number $Bo \equiv \rho g a^2 / \sigma$ measure, respectively, the relative importance of viscous and gravity forces to capillary forces. In these dimensionless numbers, σ is the surface tension, and g is the gravitational acceleration. Throughout this paper, all variables are made dimensionless with a, Q and σ.

Equations (2.1*a*) and (2.1*b*) obey the following boundary conditions. At the bubble surface, the stress satisfies

$$\boldsymbol{T} \cdot \boldsymbol{n} + p_g \boldsymbol{n} = \boldsymbol{n}(\boldsymbol{\nabla} \cdot \boldsymbol{n} - z Bo). \tag{2.1c}$$

Here, $\boldsymbol{n}$ is the unit normal outward to the gas, $\boldsymbol{\nabla} \cdot \boldsymbol{n}$ is the mean curvature, and p_g is the gas pressure relative to the liquid pressure $p(r \to \infty, z = 0)$. The gas flowing into the bubble is assumed inviscid and of negligible density. Thus, p_g is a constant; its value

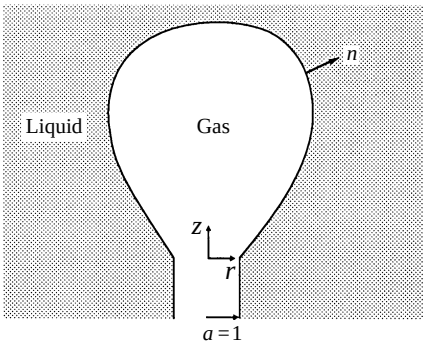

FIGURE 1. A bubble pinned at the tip of a tube.

is unknown and must be determined as part of the solution. Equation (2.1 *c*) states that the shear stress is zero at the clean bubble surface, and that the jump in the normal stress is due to the capillary pressure and the difference in the hydrostatic pressures. Further, at the bubble surface the fluid velocity must satisfy the constant flow rate condition:

$$\iint_{\Omega_B} \boldsymbol{u}\cdot\boldsymbol{n}\,\mathrm{d}S = \pm 1. \tag{2.1 d}$$

The surface integral is over the bubble surface Ω_B. The positive sign holds for bubble expansion.

On the tube surface, the fluid obeys the no-slip condition:

$$\boldsymbol{u} = 0. \tag{2.1 e}$$

At infinity,

$$\boldsymbol{u} = 0, \quad \boldsymbol{T} = 0. \tag{2.1 f, g}$$

Given a bubble shape, (2.1) yields the velocity and stress fields of the liquid, and the gas pressure. The bubble surface is then advanced by the kinematic condition:

$$\frac{\mathrm{d}\boldsymbol{X}}{\mathrm{d}t} = (\boldsymbol{u}\cdot\boldsymbol{n})\,\boldsymbol{n}, \tag{2.2}$$

where $\boldsymbol{X}$ is the position of the bubble surface and $\mathrm{d}/\mathrm{d}t$ is the derivative in the Lagrangian frame. During bubble deformation, the bubble is pinned to the rim of the tube. Thus, the contact angle is unspecified and is free to take any value as determined by the solution of the problem.

3. Boundary integral formulation

The boundary integral formulation is employed in this work to solve the Stokes flow. The formulation makes use of the linearity of the Stokes equations and superposes flow fields generated by point forces distributed on the bubble and tube surfaces. The distribution is initially unknown and is determined by imposing the boundary conditions on the superposed flow fields. Since the unknowns and the conditions needed to solve them are all located on the boundary, the dimension of the problem is reduced by one, a distinct advantage of the boundary integral formulation. In addition, the point-force solution vanishes at infinity, so the superposed flow fields already satisfy the boundary conditions at infinity. The strong emphasis of the

boundary integral formulation on the domain boundary makes it an ideal tool for problems with deforming or irregular domain boundaries, as in the present nonlinear, free-boundary problem.

For axisymmetric problems, ring force Green's functions apply and they obey

$$\boldsymbol{\nabla}\cdot\hat{\boldsymbol{T}}^{\alpha} = -\boldsymbol{\nabla}\hat{p}^{\alpha} + \nabla^2\hat{\boldsymbol{u}}^{\alpha} = -\frac{\delta(r-\hat{r})\,\delta(z-\hat{z})}{2\pi\hat{r}}\boldsymbol{e}_{\alpha} \quad (\alpha = r, z), \tag{3.1a}$$

$$\boldsymbol{\nabla}\cdot\hat{\boldsymbol{u}}^{\alpha} = 0. \tag{3.1b}$$

$\hat{\boldsymbol{T}}^{\alpha}$, $\hat{\boldsymbol{u}}^{\alpha}$, and $\hat{p}^{\alpha}$ are the stress, velocity, and pressure fields induced by a unit-strength ring force located at $(\hat{r}, \hat{z})$ and acting in direction $\boldsymbol{e}_{\alpha}, \alpha = r, z$. The superscript on the Green's function denotes the direction of the ring force. The symbol δ represents the delta function. The boundary conditions are those at infinity

$$\hat{\boldsymbol{T}}^{\alpha} \to 0, \quad \hat{\boldsymbol{u}}^{\alpha} \to 0. \tag{3.1c, d}$$

Solution of (3.1) is obtained most directly by integrating a ring of point forces (Rallison & Acrivos 1978). For completeness, the Appendix lists the six components of the stress Green's function $\hat{T}^r_{rr}$, $\hat{T}^r_{rz}$, $\hat{T}^r_{zz}$, $\hat{T}^z_{rr}$, $\hat{T}^z_{rz}$ and $\hat{T}^z_{zz}$ and the four components of the velocity Green's function $\hat{u}^r_r$, $\hat{u}^r_z$, $\hat{u}^z_r$ and $\hat{u}^z_z$.

The Green's functions lead to the solution of (2.1) through the use of the Lorentz reciprocal identity:

$$\iiint [\boldsymbol{u}\cdot(Ca\,\boldsymbol{\nabla}\cdot\hat{\boldsymbol{T}}^{\alpha}) - \hat{\boldsymbol{u}}^{\alpha}\cdot(\boldsymbol{\nabla}\cdot\boldsymbol{T})]\,\mathrm{d}V = \iint(-\boldsymbol{n})\cdot(Ca\,\boldsymbol{u}\cdot\hat{\boldsymbol{T}}^{\alpha} - \hat{\boldsymbol{u}}^{\alpha}\cdot\boldsymbol{T})\,\mathrm{d}S \quad (\alpha = r, z), \tag{3.2}$$

where the volume integration is over the liquid. The identity is derived by first rearranging the integrand of the volume integral into a divergence form (Pozrikidis 1992, p. 9). The divergence theorem then converts the volume integral into the surface integral. Substitution of (2.1*a*) and (3.1*a*) into the volume integral yields $\frac{1}{2}u_{\alpha}(\hat{r}, \hat{z})\,Ca$ when the source point (ring force) lies on the domain boundary (Ladyzhenskaya 1969). The surface integral covers the bubble surface Ω_B, the tube surface Ω_T, and the liquid surface at infinity. However, the surface integral at infinity vanishes because the integrand decreases to zero sufficiently fast far away from the bubble. Thus, (3.2) with the boundary conditions (2.1*c*) and (2.1*e*) becomes

$$\begin{aligned}\tfrac{1}{2}Ca\,u_{\alpha}(\hat{r}, \hat{z}) = &\iint_{\Omega_B} [Ca\,\boldsymbol{u}\cdot\hat{\boldsymbol{T}}^{\alpha}\cdot\boldsymbol{n} - \hat{\boldsymbol{u}}^{\alpha}\cdot\boldsymbol{n}(\boldsymbol{\nabla}\cdot\boldsymbol{n} - zBo - p_g)]\,\mathrm{d}S \\ &- \iint_{\Omega_T} \hat{\boldsymbol{u}}^{\alpha}\cdot\boldsymbol{T}\cdot\boldsymbol{n}\,\mathrm{d}S \quad (\alpha = r, z).\end{aligned} \tag{3.3}$$

Note again that the source point at $(\hat{r}, \hat{z})$ lies either on the bubble or the tube surface. Given a bubble shape (i.e. Ω_B, and hence $\boldsymbol{n}$), there are five unknowns in (3.3): the fluid velocity on the bubble surface $\boldsymbol{u} = u_r\boldsymbol{e}_r + u_z\boldsymbol{e}_z$, the stress on the tube surface $\boldsymbol{T}\cdot\boldsymbol{n} = \boldsymbol{T}\cdot\boldsymbol{e}_r = T_r\boldsymbol{e}_r + T_z\boldsymbol{e}_z$, and the gas pressure p_g. Putting successively $(\hat{r}, \hat{z})$ on the bubble surface and on the tube surface yields two equations when $\alpha = r$, and another two equations when $\alpha = z$. The constant flow rate condition (2.1*d*) determines the gas pressure p_g. Thus, we have five linear equations for the five unknowns.

Once the fluid velocity on the bubble surface is determined, the bubble is advanced by the kinematic condition (2.2). In this way, the location of the bubble, which is another unknown, is determined, and the bubble evolves.

4. Numerical method

For efficient numerical solution of (3.3), the tube length is contracted from infinity to unity by the transformation

$$x = \frac{-z}{1-z}. \tag{4.1a}$$

Equation (3.3) simplifies further when the integration in the azimuthal direction is evaluated explicitly:

$$\begin{aligned}\frac{1}{4\pi} Ca\, u_\alpha(\hat{r},\hat{z}) - \int_0^1 (T_r \hat{u}_r^\alpha + T_z \hat{u}_z^\alpha)\frac{\mathrm{d}x}{(1-x)^2} \\ - s_0\, Ca \int_0^1 [u_r(\hat{T}_{rr}^\alpha n_r + \hat{T}_{rz}^\alpha n_z) + u_z(\hat{T}_{rz}^\alpha n_r + \hat{T}_{zz}^\alpha n_z)]\, r\, \mathrm{d}s \\ = -s_0 \int_0^1 \hat{\boldsymbol{u}}^\alpha \cdot \boldsymbol{n}(\boldsymbol{\nabla}\cdot\boldsymbol{n} - zBo - p_g)\, r\, \mathrm{d}s \quad (\alpha = r, z).\end{aligned} \tag{4.1b}$$

Here, n_r and n_z are the components of $\boldsymbol{n}$. On the bubble surface, the arc length s is normalized by the total arc length $s_0 = s_0(t)$. The left-hand side of (4.1*b*) contains the unknowns u_r, u_z, T_r and T_z, and the right-hand side is the source term, which contains the gas pressure p_g. In problems where the gas pressure is specified, (4.1*b*) has sufficient equations to solve for the unknowns. Here, the gas pressure is unknown and is determined by the constant flow rate condition (2.1*d*):

$$2\pi s_0 \int_0^1 (u_r n_r + u_z n_z)\, r\, \mathrm{d}s = \pm 1. \tag{4.1c}$$

The integrals are discretized by converting each into a sum using the Gauss–Legendre quadrature, i.e. the Nystrom method (Delves & Mohamed 1985). The integrand is then evaluated at the non-uniformly distributed quadrature points. Placing successively the source point on the quadrature points yields a system of linear algebraic equations: $[A][X] = [B]$ (see Appendix B for details). The unknown vector $[X]$ consists of $2M + 2N$ elements: $u_r(x_i)$ and $u_z(x_i)$, $i = 1$ to M, and $T_r(x_j)$ and $T_z(x_j)$, $j = 1$ to N. The gas pressure p_g in the source term $[B]$ is also unknown and is found from the constant flow rate condition (4.1*c*) by the following method. First, the source term is decomposed into two known vectors: $[B] = [B_1] + p_g[B_2]$. Each of the vectors is then multiplied by the inverse of the matrix $[A]$. This gives $u_r(x_i)$ and $u_z(x_i)$, $i = 1$ to M, in terms of p_g. The velocity components are then substituted into (4.1*c*) to find p_g. This completes the solution for one timestep.

Given a bubble shape, the above numerical solution gives the fluid velocity on the bubble surface. The bubble is then advanced by the kinematic condition (2.2), implemented through a second-order Runge–Kutta scheme. For numerical stability, the maximum normal displacement Δn is fixed at each timestep. This determines the timestep $\Delta t = \Delta n / u_n^{max}$, where u_n^{max} is the maximum normal velocity at the bubble surface.

The Nystrom method is found to be more efficient than the boundary-element method for this problem. In the boundary-element method, the integral is expressed as a double sum, with the outer sum carried over the global domain and the inner over each element. Each term in the inner sum requires an evaluation of the Green's functions, which contain complete elliptic integrals and are computationally costly to

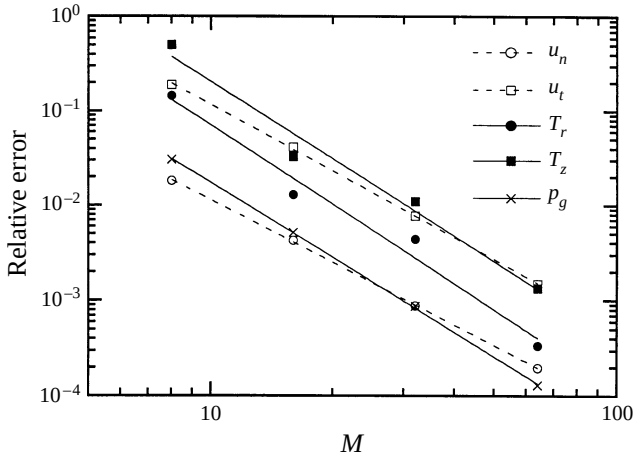

FIGURE 2. Convergence rate in the number of grid points on the bubble. At $t = 0$, a static bubble of $V = 14$ is expanded at $Bo = 0.095$ and $Ca = 1.6$. Equation (4.1) is solved with $\Delta t = 0.005$, $N = 128$, and $M = 8$, 16, 32, 64 or 128. At $t = 0.1$, we calculate the values of u_n and u_t at $s = 0.5$, T_r and T_z at $x = 0.1$, and p_g. The solutions obtained with $M = 128$ are compared with others to give the relative errors. The lines are the best power fit.

evaluate. The Nystrom method avoids this subgrid evaluation of the Green's functions. Moreover, the Nystrom method can resolve regions with high curvature by defining a new independent variable to stretch those regions so as to make efficient use of the grid points.

The analysis of the convergence rate for the Nystrom method is simpler because it has only a single sum. As an example, figure 2 shows the relative errors for the unknowns u_n, u_t, T_r, T_z and p_g as a function of M, the number of grid points on the bubble, with $N = 128$ on the needle surface. The convergence rate is close to cubic. Most cases in this paper are computed with $M = 32$, $N = 35$ and $\Delta n = 2.5 \times 10^{-3}$. To check the accuracy, two cases with extreme parameter values are computed using twice the number of quadrature points and half the maximum normal displacement. The detached bubble volumes differ by less than 1% from those calculated using the usual values of M, N and Δn (see figure 9).

5. Bubble expansion from a planar interface

This section studies the expansion of a bubble from a planar interface to the moment just before detachment. The aim is to compute the detached volume and see how it is affected by the viscous force. The results apply to bubble contacting processes that generate bubbles in viscous liquids. The Bond number Bo varies from 0.01 to 0.5, which covers the range typically encountered in experiments. The capillary number Ca varies from 0.01 to 100. This range is sufficiently wide to cover not only the case of $Ca \sim 1$, where surface tension and viscous forces are equally important, but also the asymptotic limits where only one of the forces dominates. For $Ca \ll 1$, the deforming bubble resembles closely the static bubble with $Ca = 0$ up to pinching. For $Ca \gg 1$, computed detached volumes merge smoothly into an asymptotic solution valid for $Ca \to \infty$. Thus, the whole spectrum of Ca is covered.

We also examine the effect of viscosity on the maximum bubble pressure, and develop a correlation for the maximum pressure as a function of Ca for $0.01 \leqslant Ca \leqslant 100$. This correlation enables the maximum bubble pressure method to be

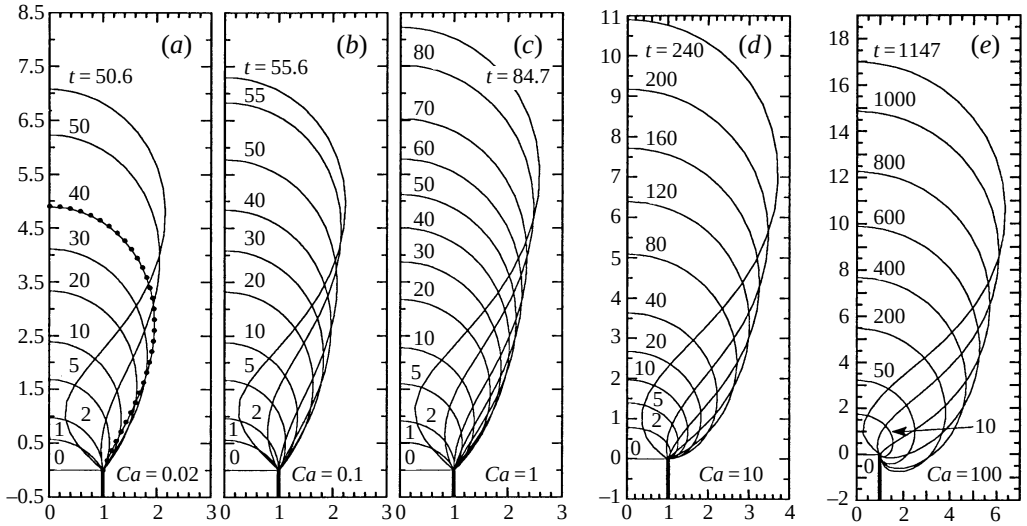

FIGURE 3. Bubble expansion at a fixed Bond number ($Bo = 0.1$) and different capillary numbers. A static bubble with volume $V = 40$ is also plotted in (*a*) in solid circles to compare with the deforming bubble. Note the change in scales for (*d*) and (*e*).

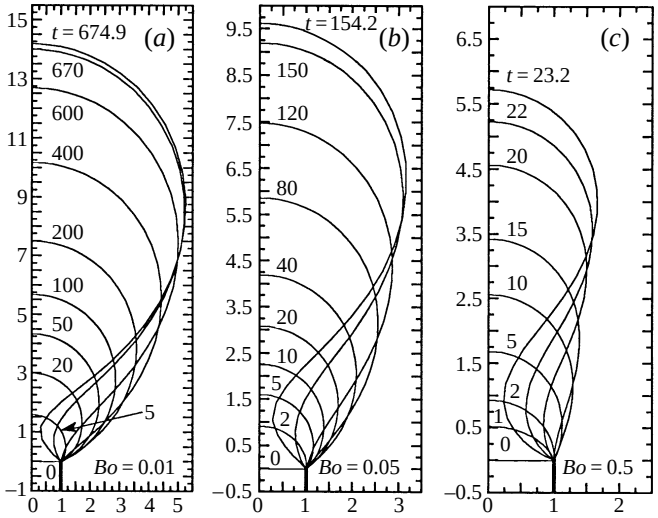

FIGURE 4. Bubble expansion at a fixed capillary number ($Ca = 1$) and different Bond numbers.

applied to viscous liquids for which the dynamic tension no longer equals the maximum pressure multiplied by $\frac{1}{2}a$. Finally, computed surface tangential velocities shed light on surfactant convective transport on bubbles deforming in a surfactant solution. The information could help to improve the maximum bubble pressure and pendant bubble methods. In this section, the time t can be taken as the bubble volume V because $\mathrm{d}V/\mathrm{d}t = 1$ and the bubble starts from zero volume.

5.1. *General features*

Before the main results are presented, it is instructive to look at the general features of the solutions. Figures 3 and 4 show the evolution of bubbles from a flat interface to an elongated pendant shape with a thin neck. In figure 3 the Bond number is 0.1 for the

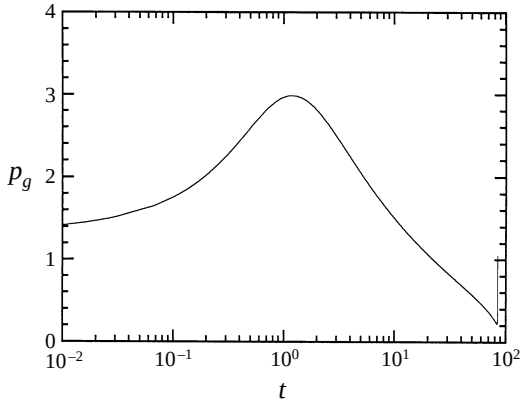

FIGURE 5. The gas pressure as a function of time for the bubble in figure 3(*c*). $Bo = 0.1$, $Ca = 1$.

five bubbles, whereas in figure 4 and capillary number is kept constant ($Ca = 1$). Thus, these figures represent two cross-sections of the parameter space. Figure 3 shows that as Ca increases, the bubble detaches at a larger size. This increases in bubble size is also present in figure 4 as Bo decreases. (We derive later that the detached bubble volume varies as $(Ca/Bo)^{3/4}$ as $Ca/Bo \to \infty$.) A static bubble of $V\,(=t) = 40$ is also plotted in figure 3(*a*). It shows that a bubble expanding at $Ca = 0.02$ looks the same as the static bubble up to the onset of pinch off. At high Ca, the bubble grows around the tube edge and seems to fold over towards the back of the tube. This change in bubble shape is not observed in figure 4, where the shape sequences of all bubbles resemble each other except for the differences in size.

The evolution of the bubble can be explained as follows. As a bubble first emerges from a tube, gravity is relatively unimportant because the bubble is small. The initial bubble shape is therefore governed by viscous and capillary forces. The capillary force alone would form a spherical bubble, with the tip of the tube at one side of the bubble. As the liquid becomes more viscous, the bubble tends to grow radially from the tube tip. Thus, figure 3 shows that as Ca increases, the bubble loops around the tube tip and grows increasingly more towards the back of the tube. As the bubble grows larger, the gravity force eventually takes over and pulls the bubble off the tube.

The five unknowns p_g, u_n, u_t, T_r, and T_z are presented next for the bubble in figure 3(*c*) to illustrate the general features. Figure 5 shows the evolution of the gas pressure. At $t = 0$, the interface is flat, but the gas pressure is non-zero because a finite pressure is needed to push the viscous liquid away to form a bubble. As the bubble grows, its mean curvature increases and reaches a maximum when the bubble becomes roughly hemispherical. At $Ca = 1$, part of the gas pressure balances the capillary force, which is proportional to the mean curvature. Thus, the gas pressure also exhibits a maximum. As the bubble grows beyond a hemisphere, the overall mean curvature decreases monotonically, and so does the bubble pressure. This decrease continues until the onset of pinch-off, at which point the calculated gas pressure increases rapidly. This rapid increase can be explained as follows. At the beginning of pinch-off, the liquid hydrostatic pressure increases from the bubble apex to the base, and eventually the difference becomes sufficiently large that the bubble begins to neck. As the neck thins, the increasing circumferential curvature develops a large capillary pressure locally at the neck, which drives the subsequent motion of the neck. Since p_g is declining, the liquid pressure adjacent to the neck decreases. The resulting $\partial p/\partial r$ is balanced by viscous

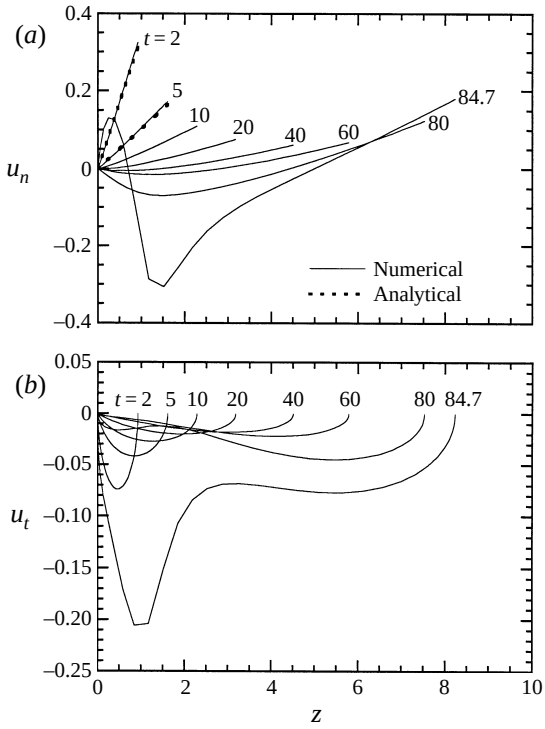

FIGURE 6. (*a*) The normal and (*b*) the tangential surface velocities for the bubble in figure 3(*c*). The dashed lines are the analytical solution (5.4). No curve smoothing has been applied. $Bo = 0.1$, $Ca = 1$.

forces that arise as liquid flows towards the neck to precede snap-off (figure 6(*a*)). As the neck shrinks further, this liquid flow cannot produce large enough viscous forces (figure 6, $t = 80$, velocity gradients are too small). So, the Stokes equations, which require the viscous and pressure forces to balance, limit $\partial p/\partial r$ and thus the depression in the liquid pressure adjacent to the neck. The only way to balance the rapidly increasing capillary pressure is by raising the calculated gas pressure, as in figure 5.

We note that the large liquid acceleration at the neck could lead to locally large inertial effects. Fluid inertia retards the acceleration and acts to balance the circumferential capillary driving force, so the increase in bubble pressure in figure 5 would be less rapid if not eliminated. The sharp turn depicted in figure 5 is due to the logarithmic compression of the time units. The calculated rate of change of gas pressure during pinch-off is about the same as that during the initial bubble formation.

Figure 6 plots the normal and tangential surface velocities u_n and u_t as a function of z for the bubble in figure 3(*c*). (u_n is positive outward from the bubble, and u_t is positive pointing from the bubble apex to the base.) As shown in figure 6(*a*), u_n varies linearly with z at early times. This linear behaviour can be predicted analytically by noting from figure 3(*c*) that the bubble emerges roughly as part of a sphere. Consider a spherical bubble of instantaneous radius $R(t)$ with its centre at $r = 0$ and $z = z_0(t)$, where (r, z) are the cylindrical coordinates defined in figure 1. As the bubble expands radially with velocity $\mathrm{d}R/\mathrm{d}t$ and rises with velocity $\mathrm{d}z_0/\mathrm{d}t$, it has at its surface a normal velocity

$$u_n = \frac{\mathrm{d}R}{\mathrm{d}t} + \frac{\mathrm{d}z_0}{\mathrm{d}t}\left[\frac{\pm(R^2 - r^2)^{1/2}}{R}\right]. \tag{5.1}$$

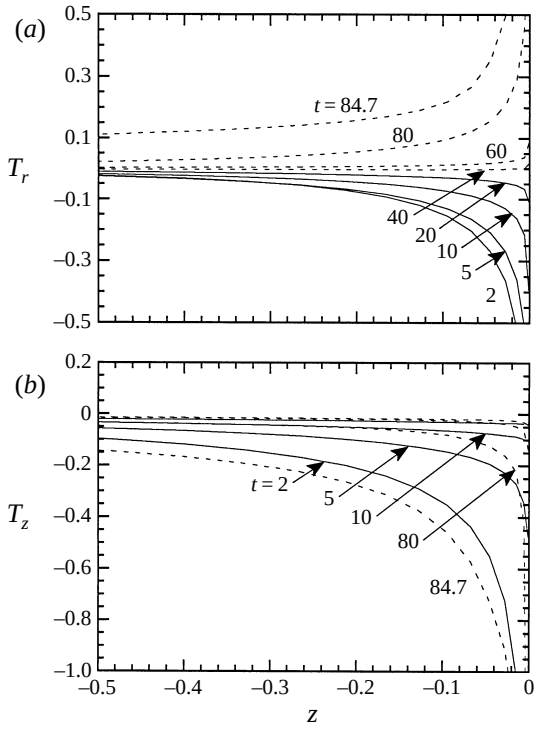

FIGURE 7. (*a*) The normal and (*b*) the tangential stresses at the tube surface for the case in figure 3(*c*). $Bo = 0.1$, $Ca = 1$.

The positive sign holds for the upper hemisphere and the negative sign for the lower. The condition that the bubble is pinned at the tube tip requires $u_n = 0$ at $r = 1$ and $z = 0$. This gives $\mathrm{d}z_0/\mathrm{d}t$ in terms of $\mathrm{d}R/\mathrm{d}t$, and (5.1) becomes

$$u_n = \frac{-z}{\pm(R^2-1)^{1/2}}\frac{\mathrm{d}R}{\mathrm{d}t}, \tag{5.2}$$

where z is the vertical distance from the tube tip (figure 1). The radial velocity $\mathrm{d}R/\mathrm{d}t$ is found from $\mathrm{d}V/\mathrm{d}t = 1$ and

$$V = \tfrac{1}{3}\pi(2R \pm (R^2-1)^{1/2})(\pm(R^2-1)^{1/2} - R)^2. \tag{5.3}$$

Substitution of $\mathrm{d}R/\mathrm{d}t$ into (5.2) gives

$$u_n = \frac{z}{\pi R(\pm(R^2-1)^{1/2} - R)^2}. \tag{5.4}$$

This velocity profile is plotted in figure 6(*a*) for $t\ (= V) = 2$ and 5. The excellent agreement thus explains the linear velocity profiles, and confirms the validity of the numerical code in this particular situation. As the bubble approaches detachment, u_n at the neck becomes negative and increases rapidly. The tangential velocity u_t is always negative as shown in figure 6(*b*), indicating that the liquid flow near the bubble is always upward. Again, as the bubble approaches detachment, u_t at the neck increases rapidly. The velocities at $t = 84.7$ show that the lengthscale over which u_n and u_t vary is about the same as the grid spacing. At this point, the grids are not fine enough to resolve the rapid variation of u_n and u_t, and the numerical solution becomes unreliable.

Figure 7 plots the normal and shear stresses T_r and T_z on the tube wall for the case shown in figure 3(*c*). The normal stress is unbounded at the tube tip and changes sign

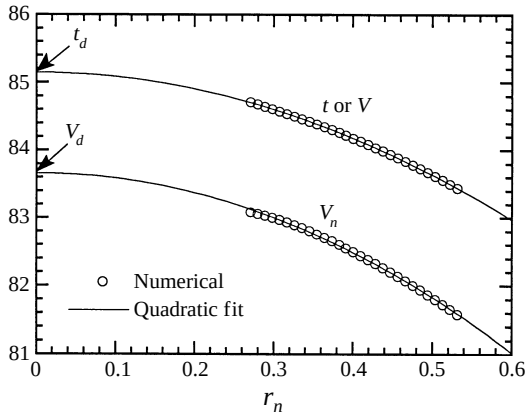

FIGURE 8. Bubble volumes versus the neck radius for the bubble in figure 3(*c*). V_n is the volume above the neck, whereas $V (= t)$ is the total bubble volume. The circles are the numerical solutions and the curves are the best quadratic fit described in (5.5). $Bo = 0.1$, $Ca = 1$.

at $t \approx 30$. This can be explained by the hinged motion of the bubble surface near the pinned contact line. Figure 3(*c*) shows that the bubble surface pivots about the contact line, so the contact angle in the liquid side varies. For $t < 30$, the contact angle decreases, and the liquid around the contact line is squeezed. The contact angle reaches minimum at $t \approx 30$, as shown by the bubble shapes in figure 3(*c*) and by the normal surface velocity profiles in figure 6(*a*). The contact angle then increases, which creates suction that draws liquid towards the contact line. Variation in the contact angle generates unbounded liquid pressures at the contact line, as indicated by the local solutions of Moffatt (1964), who considered Stokes flow in a wedge driven by either closing or opening the wedge. One side of the wedge wall obeys no-slip and the other side obeys no-stress. He found that the pressure at the corner (contact line) becomes positively unbounded during squeezing and negatively unbounded during expansion. This explains why the normal stress is negatively unbounded at the tube tip at $t < 30$, passes through zero at $t \approx 30$, and becomes positively unbounded at $t > 30$. The shear stress at the tube tip is also unbounded because of a sudden change in the boundary condition from no-slip on the tube wall to no-stress on the bubble (Schultz & Gervasio 1990; Anderson & Davis 1993; Salamon *et al.* 1995). The shear stress is negative for all times because an expanding bubble acts as a source and drives liquid radially away from the tube tip. Moffatt (1964) also studied Stokes flow around the tip of a wedge driven by a source away from the tip. The wedge angle was fixed. He found that the shear stress is regular at the tip for wedge angles $\leqslant 120°$. For wedge angles $> 120°$, the shear stress is singular and the order of singularity increases with the contact angle. This explains why the shear stress in figure 7(*b*) is regular at $t \approx 30$ when the contact angle reaches a minimum value of roughly 120°. Moreover, the magnitude of the singularity depends on the magnitude of the liquid flow around the contact line. Fluid motion near the contact line is weakest at $t \approx 30$ as shown in figures 6(*a*) and 6(*b*). This further explains the collapse of the shear stress around $t \approx 30$ in figure 7(*b*).

Salamon *et al.* (1995) studied numerically the singularity induced by a sudden change in the boundary condition from no-slip to no-stress. They modelled the exit flow at the end of a two-dimensional channel, i.e. the die-swell problem. They verified that the liquid surface approaches the contact line with unbounded curvature, as first suggested by Schultz & Gervasio (1990). The size of this singular region vanishes as $Ca \to 0$; it is roughly 0.05 of the channel height for $Ca = 100$ and it decreases rapidly to 10^{-5} of the

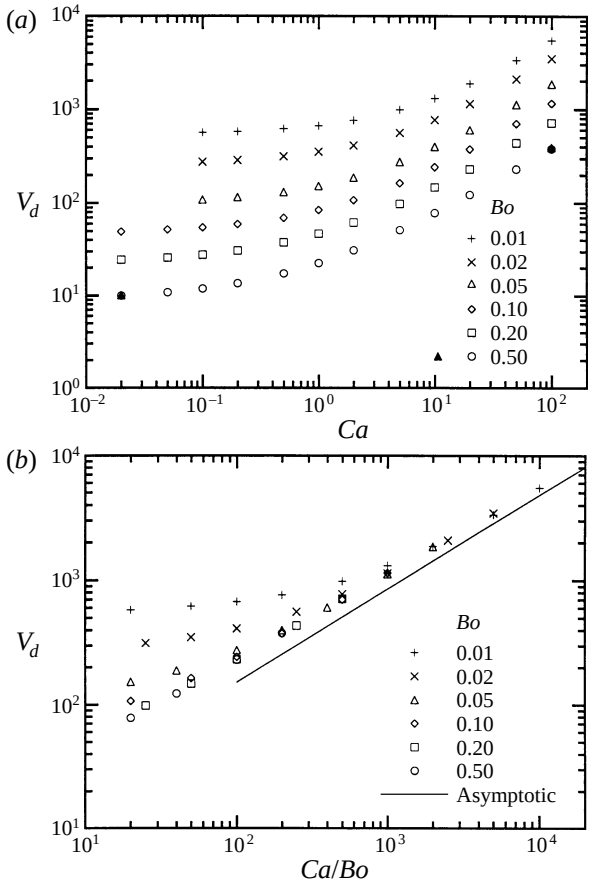

FIGURE 9. (*a*) The detached bubble volume as a function of the capillary number for various Bond numbers. The solid triangles are obtained with double the grid points and half the maximum normal displacement per time step. (*b*) The asymptotic behaviour of the detached bubble volume. The asymptotic solution is given in (5.10).

channel height for $Ca = 0.1$. Most importantly, Salamon *et al.* (1995) showed that failure to capture the unbounded surface curvature has no effect on the bulk flow away from the singular region. Thus, the numerical solutions presented here are accurate even when the singular region is much smaller than the resolution of the numerical scheme.

5.2. *Detached bubble volume*

The detached bubble volume V_d is determined here by extrapolation. By definition, V_d is the volume above the neck as the neck pinches off. However, the numerical solution, owing to its limited resolution, cannot follow the bubble evolution to zero neck radius. A consistent way of finding V_d is to express the volume V_n above the neck as a function of the neck radius r_n, and extrapolate to zero r_n. Figure 8 shows such an extrapolation for the bubble in figure 3(*c*). We find that the quadratic fit

$$V_n(r_n) = V_n(0) + O(r_n^2) \tag{5.5}$$

describes very well the behaviour of $V_n(r_n)$, and we use it to find the detached bubble volume $V_d = V_n(0)$ for all bubbles.

The detached bubble volume is plotted against the capillary number in figure 9(*a*)

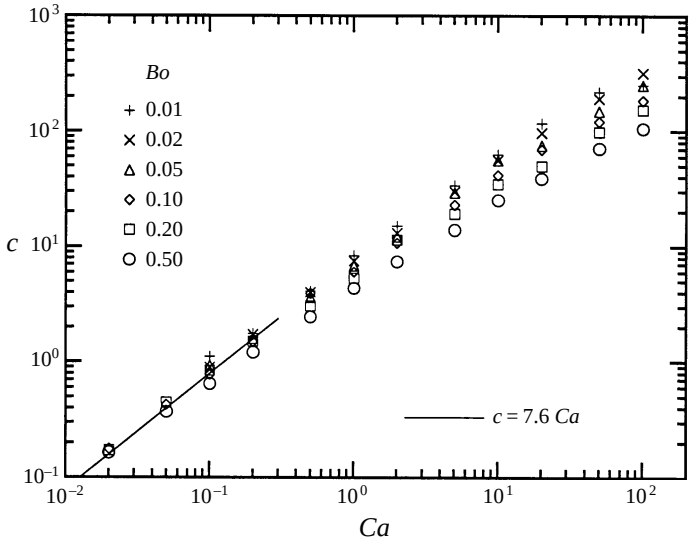

FIGURE 10. The fitting constant defined in (5.6) as a function of the capillary number for various Bond numbers.

for various Bond numbers. The data show clearly two different regimes at the zero and infinite limits of Ca, indicating that two different mechanisms are responsible for breaking off the bubble. At low Ca, a growing bubble resembles the static bubble (figure 3(*a*)). Given Bo, the static bubble has a maximum volume beyond which no static solution exists (Longuet-Higgins *et al.* 1991; Michael 1981). Thus, when a bubble grows beyond the maximum static volume, snap-off ensues. The amount of gas that can enter the bubble during pinching depends on the pinching time, which can be estimated by the following methods.

One estimate of the pinching time comes from the numerical solution of necking. Figure 8 shows how the neck radius r_n decreases with time t during pinching for the bubble in figure 3(*c*). If we define t_d as the time the neck pinches off, then from figure 8,

$$t = t_d - cr_n^2 \quad \text{as} \quad r_n \to 0. \tag{5.6}$$

This quadratic behaviour is also found in Longuet-Higgins *et al.* (1991) and Oguz & Prosperetti (1993). At the beginning of pinching, $r_n \approx 1$. Thus, the fitting constant c in (5.6) measures roughly the time that the neck shrinks from $r_n \approx 1$ to $r_n = 0$, i.e. the pinching time. Figure 10 plots c as a function of Ca for various Bo. The data show that as $Ca \to 0$, $c \to 7.6Ca$, independent of Bo. This linear behaviour arises because the bubble shape from which pinching starts becomes independent of Ca as $Ca \to 0$, and because the pinching time is controlled by viscous forces; during pinching the driving capillary force (circumferential curvature) can only be balanced by viscous forces, even in the limit $Ca \to 0$ (see §5.4). The constant of proportionality is independent of Bo because pinching is a local event and because the neck radius of the marginally stable static bubble is insensitive to Bo (Longuet-Higgins *et al.* 1991). This explains the behaviour of c observed in figure 10.

This estimate of the pinching time can also be derived from the growth rate of an unstable perturbation. A static bubble with the maximum allowable volume is unstable to infinitesimal perturbations. The growth rate of an unstable perturbation is proportional to $\sigma/a\mu$, which is the same as that of an unstable perturbation to a viscous liquid thread (Chandrasekhar 1961). By assuming that the nonlinear effects do not slow

the pinching significantly, the pinching time, made dimensionless by a^3/Q, is $\mu Q/\sigma a^2 = Ca$. Thus, as $Ca \to 0$, the amount of gas that enters the bubble during pinching is $O(Ca)$. We therefore expect that the calculated total bubble volume at detachment and the detached volume should be bounded from below and approach the static total and detached volumes as $Ca \to 0$. (The static detached volume is defined as the volume above the neck at the maximum volume.) Table 1 lists the detached volume and total bubble volume at detachment for $Ca = 0.02$ to 100 and $Bo = 0.01$ to 0.5. The static results are determined by a numerical solution of the Young–Laplace equation, and are accurate to four significant figures. For $Bo = 0.01$, where a direct comparison is possible, our static results agree with that of Longuet-Higgins *et al.* (1991) to within 0.5%. We note from the table that for the lowest values of Ca ($= 0.02$) the detached and total volumes are still a few per cent larger than the static values. We expect smaller differences (≈ 0.02) at this value of Ca. We note that this difference is not due to numerical error; we have recomputed the case with $Bo = 0.5$ and $Ca = 0.02$ with double the number of grid points and half the maximum displacement per timestep, and obtained the same total and detached volumes.

At high Ca, the detached bubble volume is determined by a balance between buoyancy and viscous forces. To derive an analytic solution valid for high Ca, we consider the motion of a spherical bubble expanding radially with unit volume expansion rate (i.e. $\mathrm{d}V/\mathrm{d}t = 1$), and subject to buoyancy and viscous forces. At each instant, a balance of the forces in the vertical direction gives (Davidson & Schuler 1960*b*)

$$Bo\, V = 4\pi\, Ca\, UR, \tag{5.7}$$

where V is the volume of the bubble, U its translational velocity, and R its radius. Thus, $R = (3V/4\pi)^{1/3}$, and $U = \mathrm{d}z_0/\mathrm{d}t = \mathrm{d}z_0/\mathrm{d}V$, where z_0 is the vertical displacement of the bubble centre. Substitution into (5.7) gives

$$\frac{\mathrm{d}z_0}{\mathrm{d}V} = \frac{1}{(4\pi)^{2/3}\, 3^{1/3}} \frac{Bo}{Ca} V^{2/3}. \tag{5.8}$$

The solution of this equation with the initial condition that $z_0 = 0$ at $V = 0$ is

$$z_0 = \frac{1}{5}\left(\frac{3}{4\pi}\right)^{2/3} \frac{Bo}{Ca} V^{5/3}. \tag{5.9}$$

We define the detached bubble volume V_d as the volume when $z_0 = R$. Thus,

$$V_d = \left(\frac{4\pi}{3}\right)^{1/4} \left(\frac{5Ca}{Bo}\right)^{3/4}. \tag{5.10}$$

Because (5.10) is derived in the absence of a tube, it is valid only for $V_d \gg 1$ or $Ca/Bo \to \infty$ (i.e. $a \to 0$). Figure 9(*b*) plots V_d versus Ca/Bo for various Bo. At high Ca/Bo, the data with different Bo collapse into a single curve and approach the asymptotic solution. Thus, the detached bubble volume is found for $0 < Ca < \infty$.

5.3. *Maximum gas pressure p_m*

In using the maximum bubble pressure method for measuring dynamic surface tension, viscous forces are always present but neglected. To apply the method to more viscous liquids, it is necessary to determine the effects of viscous forces on the maximum

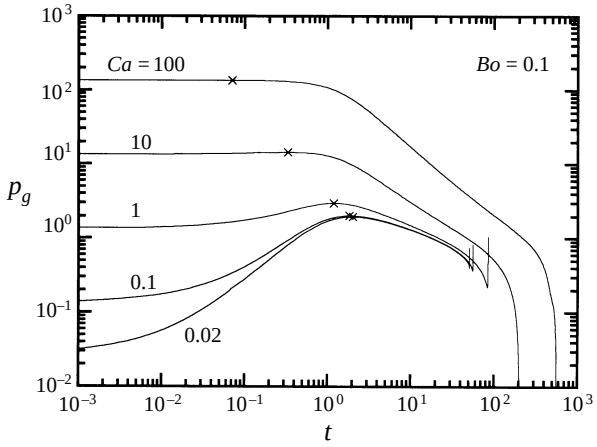

FIGURE 11. Evolution of the gas pressure for the five bubbles in figure 3. The × symbol marks the peak.

	$V_d/V(t_d)$					
Ca	*Bo*					
	0.01	0.02	0.05	0.1	0.2	0.5
100	5468/5498	3452/3471	1857/1868	1152/1160	714/719	377.4/380.0
50	3330/3349	2089/2102	1125/1132	701/706	436/439	230.8/232.7
20	1867/1878	1142/1149	604/609	375/379	232/234	123/125
10	1306/1314	774/780	398/401	243/246	149/151	78.3/79.3
5	987/994	562/567	276/279	164/166	98.7/100	51.0/52.0
2	762/767	411/414	188/191	107/109	61.9/63.5	31.0/31.8
1	671/676	351/354	153/155	83.7/85.2	46.9/48.0	22.6/23.4
0.5	620/625	314/317	131/133	69.6/71.0	37.7/38.8	17.4/18.2
0.2	577/581	287/289	115/117	58.9/60.3	30.7/31.8	13.5/14.3
0.1	564/568	275/277	109/110	54.4/55.7	27.7/28.8	11.9/12.6
0.05	—	—	—	51.6/52.9	25.9/27.0	10.8/11.6
0.02	—	—	—	49.4/50.6	24.4/25.5	9.96/10.8
[1]Static	531.1/531.2	256.9/257.0	98.24/98.44	47.59/48.00	23.01/23.80	8.432/9.835

[1] Volume above the neck/total bubble volume for the largest allowable static bubbles.

TABLE 1. Detached bubble volume V_d and total bubble volume at detachment $V(t_d)$

pressure. Figure 11 plots the gas pressure as a function of time for the five bubbles in figure 3. The curves all exhibit a maximum, the magnitude of which increases with *Ca*. The relation between the maximum gas pressure p_m and *Ca* is shown more explicitly in figure 12, which plots the difference between p_m and its static value p_s (i.e. p_m at $Ca = 0$) against *Ca* for $Bo = 0.01$, 0.1 and 0.5. (The static maximum pressure p_s depends on *Bo*; its values for $Bo = 0.01$, 0.1 and 0.5 are listed in figure 12.) Interestingly, the data for different *Bo* collapse into a single curve and are well fitted by an essentially linear power law:

$$p_m(Bo, Ca) = p_s(Bo) + 1.11\, Ca^{1.04}. \tag{5.11}$$

It seems that the gravity force affects only the static maximum pressure p_s, but has no effect on the difference between the dynamic and static maximum pressures. This simple power fit holds for $0.01 \leqslant Ca \leqslant 100$ and $0.01 \leqslant Bo \leqslant 0.5$, and is likely to be

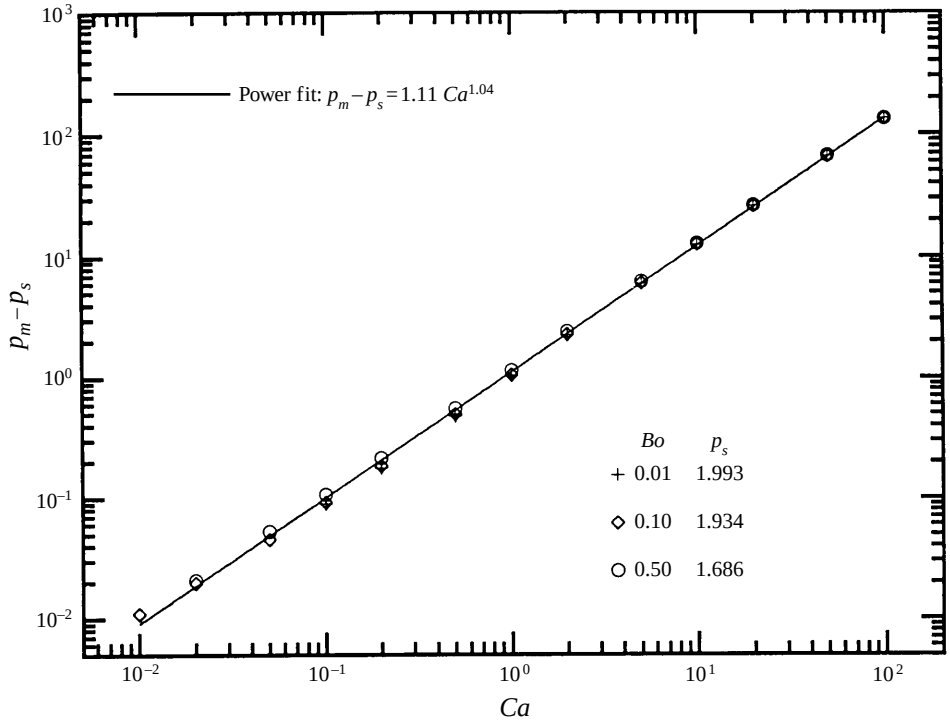

FIGURE 12. The difference between the maximum gas pressure p_m and its static value p_s (i.e. p_m at $Ca = 0$) as a function of the capillary number. Three values of p_s obtained from a numerical solution of the Young–Laplace equation are also listed.

valid for wider ranges of Ca and Bo. Thus, the maximum bubble pressure method can be used for the measurement of dynamic tension in viscous liquids where the maximum pressure is not simply given by $p_s(Bo)$.

Figure 11 shows that as Ca increases the gas pressure peaks at earlier times, and the peak is less pronounced. This can be explained by considering two limiting cases of $Ca \to 0$ and $Ca \to \infty$. As $Ca \to 0$, the gas pressure for small Bo reaches maximum when the bubble is roughly hemispherical at $t\,(= V) \approx \frac{2}{3}\pi$ with a value $p_m \approx 2$. As $Ca \to \infty$, the maximum gas pressure occurs at $t = 0$. This is because with zero surface tension the gas pressure is balanced mainly by the normal viscous stress at the bubble surface, as shown by (2.1 *c*). The normal viscous stress scales with the normal surface velocity u_n, which is largest at $t = 0$ to satisfy the constant flow rate condition. Thus, the viscous resistance is largest at $t = 0$. The initial gas pressure at $t = 0$ is found from the numerical solution as $p_g = 1.35\,Ca$, for $0 < Ca < \infty$ (see § 5.4). Thus, as $Ca \to \infty$, the maximum gas pressure occurs at $t = 0$ and its magnitude varies linearly with Ca. Figure 11 reflects the transition between the zero and infinite Ca limits.

5.4. *Singular time domains in the limit* $Ca \to 0$

In the limit $Ca \to 0$, viscous forces are negligible compared with capillary forces during growth of a bubble, except in the beginning $t \sim Ca$ and in the end $t_d - t \sim Ca$ during which the two forces become comparable. (t_d is the time for the bubble to detach.) These two singular time domains are discussed separately.

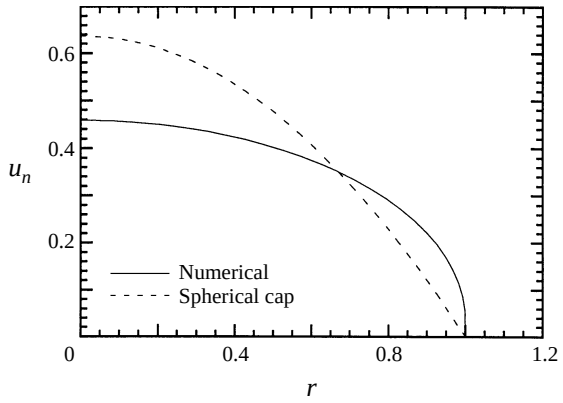

FIGURE 13. Normal surface velocities at $t = 0$. The numerical solution is independent of Ca or Bo. The spherical cap solution is given in (5.13).

5.4.1 *Start-up singularity*

As a static bubble starts to expand at $t = 0$, viscous forces completely govern the motion of the bubble even in the limit $Ca \to 0$. This is shown by the normal stress balance in (2.1 *c*):

$$p_g - p + Ca\, \boldsymbol{n}\cdot\boldsymbol{\nabla u}\cdot\boldsymbol{n} = \boldsymbol{\nabla}\cdot\boldsymbol{n}. \tag{5.12}$$

At $t < 0$, the bubble is in equilibrium, so $p = -zBo$ and $p_g + zBo = \boldsymbol{\nabla}\cdot\boldsymbol{n}$. At $t = 0$, the gas pressure p_g increases by Δp_g to deliver a unit volume flow rate. The liquid pressure at the bubble surface increases instantaneously by $\Delta p = \Delta p(s)$, but the bubble shape remains the same and will take some time to adjust to the new gas pressure. The normal stress balance at $t = 0$ reads

$$\Delta p_g = \Delta p - Ca\, \boldsymbol{n}\cdot\boldsymbol{\nabla u}\cdot\boldsymbol{n}. \tag{5.13}$$

Thus, at $t = 0$ the capillary force $\boldsymbol{\nabla}\cdot\boldsymbol{n}$ drops out completely, and the step change in gas pressure is balanced by only the normal stress in the liquid. To illustrate this point explicitly, figure 13 graphs the computed normal surface velocity at $t = 0$. This same velocity profile is obtained for different Ca, and for different Bo because the bubble surface is initially flat. On the same figure is also plotted the normal velocity of a bubble growing as part of a sphere, which is the shape of the bubble when the capillary force dominates. This normal velocity profile is parabolic:

$$u_n = \frac{2}{\pi}(1 - r^2), \tag{5.14}$$

as determined from (5.4) by substituting the function $z = z(r)$ that describes a hemisphere of radius R, and taking the limit $R \to \infty$. The computed normal velocity profile is clearly not parabolic, indicating that the viscous force dominates the capillary force at $t = 0$.

The singular start-up time where viscous forces dominate lasts for only $t \sim Ca$. This is shown again by the normal stress balance. In time t, the normal displacement of the bubble surface is $\Delta n \sim u_n t \sim t$ because $u_n \sim 1$, as required by the unit flow rate condition (4.1 *c*). The computed normal velocity in figure 13 is also the bubble shape at $t = \Delta t$, which differs from the static bubble shape (i.e. spherical cap). This difference generates a capillary force: $\Delta(\boldsymbol{\nabla}\cdot\boldsymbol{n}) \sim \Delta n/\Delta s^2 \sim \Delta n \sim t$, where $\Delta s \sim 1$ is the lengthscale

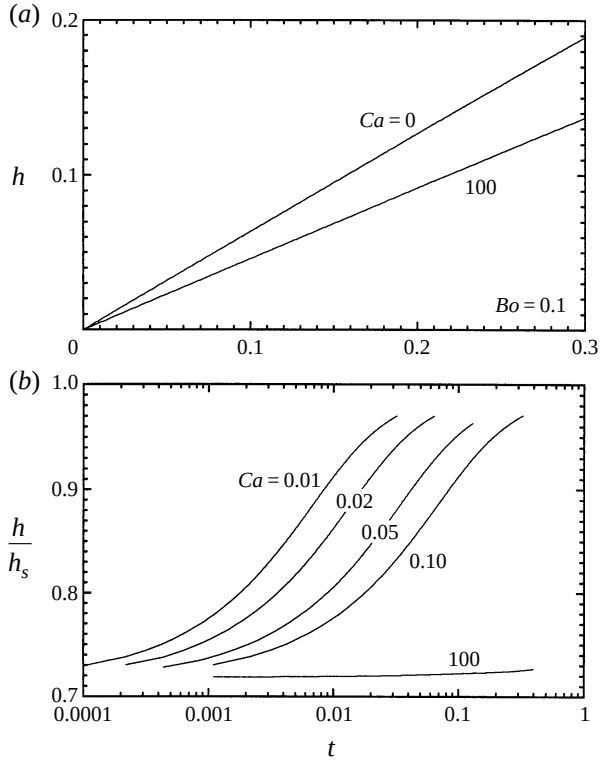

FIGURE 14. (*a*) Bubble height versus time (volume) for the static bubble and for a bubble expanding at $Ca = 100$. (*b*) Ratio of bubble height to static bubble height (h_s) versus time for various Ca to demonstrate the transition timescale.

of the arc length s. Thus, if $t \sim Ca$, the capillary and viscous terms in (5.12) are comparable, and they balance the pressure jump ($\sim Ca$) across the bubble surface. For $t \gg Ca$, the bubble surface advances by $\Delta n \sim t$, so both the capillary term and the pressure jump must change by $O(t)$. The viscous force, however, remains $O(Ca)$ as shown in (5.12). Thus, for $t \gg Ca$, the bubble motion is governed by the capillary force. This transition from viscous to capillary force dominated motion is shown explicitly in figure 14. In figure 14(*a*), the bubble height h is plotted as a function of time for two extreme cases: $Ca = 0$ and 100. The static bubble height (h_s) can be varied as a function of time because here time is equivalent to bubble volume. Figure 14(*b*) plots the ratio h/h_s as a function of time for five bubbles with $Ca = 0.01$, 0.02, 0.05, 0.1 and 100. It shows that all the curves start from the curve for $Ca = 100$, which is dominated by viscous forces. At later times, the curves merge into the static curve, which is dominated by capillary forces. For a bubble expanding at a given small Ca, the transition finishes at $t \sim Ca$, in agreement with the above scaling argument. The results shown in figure 14 are computed using $Bo = 0.1$, but this transition at $t \sim Ca$ is also observed for other Bo. We would like to emphasize that the existence of this start-up singularity is independent of the initial bubble shape. The conclusions hold for initial static shapes that are not planar.

At $t = 0$, the step change in gas pressure Δp_g varies linearly with Ca. Owing to the start-up singularity, the capillary force vanishes at $t = 0$. The Stokes problem then reduces to one without surface tension. For such a quasi-static Stokes flow, the velocity

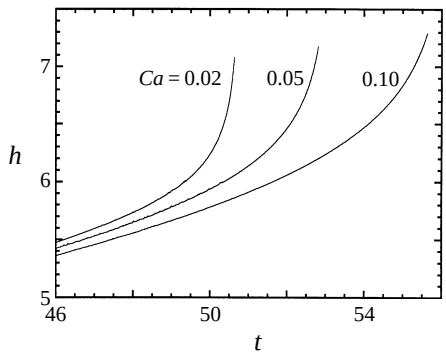

FIGURE 15. Bubble height versus time near detachment. $Bo = 0.1$.

field is independent of viscosity, and the stresses are proportional to viscosity. Thus, at $t = 0$ the normal and tangential surface velocities are independent of Ca (figure 13), but the step change in gas pressure and the stresses on the tube wall are proportional to Ca. These predictions are all confirmed by the numerical solutions. Particularly, the step change in gas pressure at $t = 0$ obeys

$$\Delta p_g = 1.35\, Ca, \tag{5.15}$$

which holds for $0 < Ca < \infty$. In this problem, $p_g = \Delta p_g$ at $t = 0$ because the bubble surface is initially flat.

5.4.2. *Pinching singularity*

In the limit $Ca \to 0$, viscous forces are also important near the end of bubble formation in time $t_d - t \sim Ca$, as discussed in § 5.2. Here, we focus on the bubble height and see how it is affected by this singular time domain. Figure 15 plots the bubble height as a function of time to compare the rate of pinch-off at different Ca. Large pinch-off rates are signified by steep increases in the apex height. As the capillary number decreases, the pinch-off process accelerates. Note that the pinch-off rate is significantly faster for $Ca = 0.02$ than for $Ca = 0.1$. Figure 16 provides a different perspective on the effect of viscosity on pinch-off at low Ca. The bubble height at $V = 10$ is plotted as a function of Ca for different Bo. At high Ca, the data for different Bo collapse into a curve as the buoyancy force is negligible at this bubble volume compared to viscous forces. As Ca decreases, the bubble heights for $Bo \leqslant 0.2$ approach the static values, but the data for $Bo = 0.5$ do not seem to be reaching a plateau. At $Bo = 0.5$, the maximum allowable static bubble volume is 9.835 (table 1). Thus, the bubble will detach before it reaches $V = 10$ as $Ca \to 0$. However, the bubble expanding at $Ca = 0.02$ has not detached at $V = 10$ as the detached bubble volume at $Ca = 0.02$ is greater than 10 (table 1). Thus, the case with $Bo = 0.5$ shows that as Ca decreases the viscous force is weaker and the bubble is closer to detachment.

6. Bubble contraction

This section presents numerical simulations for bubble contraction from a static pendant shape. Pendant bubble contraction is important in the pendant-bubble method for the measurement of dynamic surface tension owing to surfactant exchange at the bubble surface. As mentioned in § 1, the pendant bubble method forms a bubble

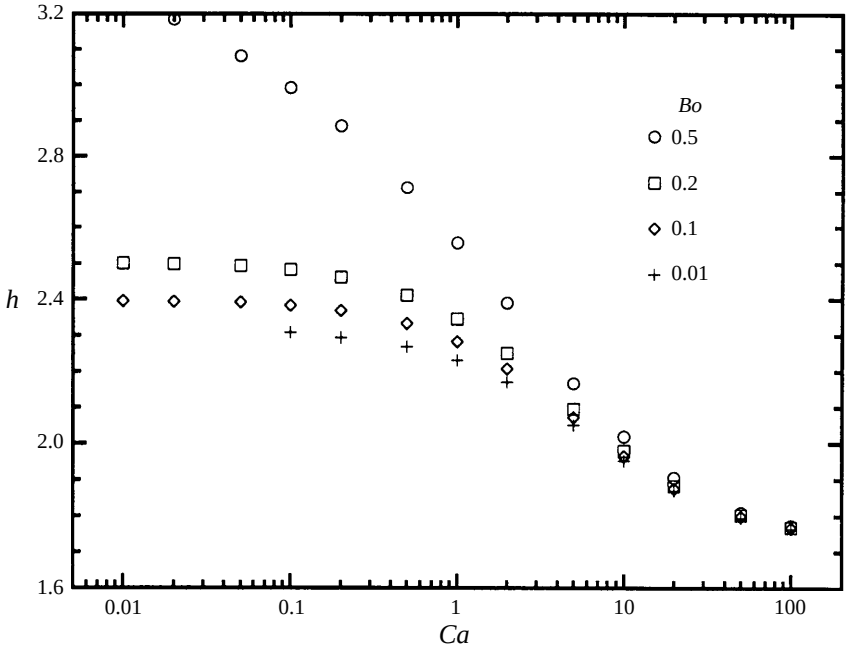

FIGURE 16. Bubble height at a particular bubble volume ($V = 10$) as a function of Ca.

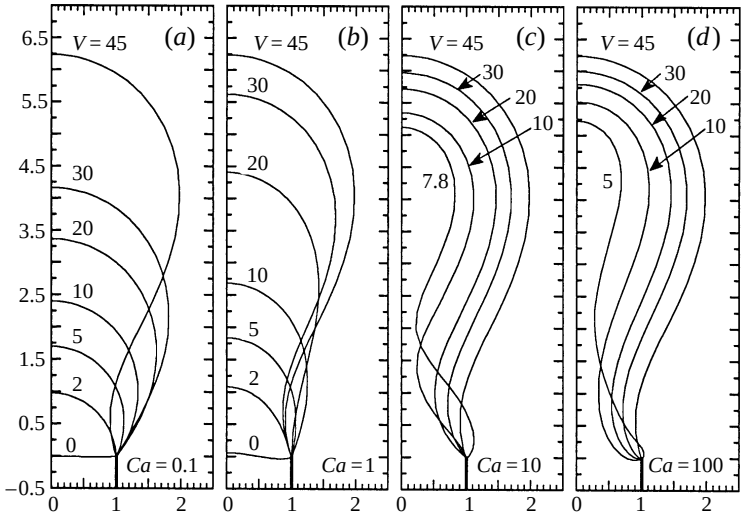

FIGURE 17. Bubble contraction at a fixed Bond number ($Bo = 0.1$) and different capillary numbers.

in a surfactant solution, and waits until an equilibrium monolayer adsorbs onto the surface. The bubble is then expanded or contracted at low capillary numbers, causing kinetic and diffusive exchange of surfactant between the bulk and surface. The surface tension at each instant is determined by fitting the digitized bubble image to the Young–Laplace solutions. The dynamic tension is a vehicle for studying surfactant transport.

Figure 17 plots the contraction of four bubbles at $Bo = 0.1$ and $Ca = 0.1$, 1, 10 and

100. The bubbles start from the same static bubble shape and volume ($V = 45$). For the two low Ca runs, the bubble retracts smoothly back to the tube. However, for the other high Ca runs, the simulations suggest that the bubbles snap off. This is because at high Ca, the normal viscous force compresses the surface of the elongated bubble, and the neck of the bubble vanishes faster than the head. The surface tension at high Ca is too weak to pull the bubble back, and a small bubble is left behind. We have observed this bubble break-up in experiments, as described below in §7. Tanveer & Vasconcelos (1995) have predicted similar break-up for two-dimensional bubbles contracting in Stokes flow.

Our simulations indicate that for $Ca \leqslant 0.1$ the bubble retracts smoothly into the tube following essentially the shape of the static bubble. Hence, it is valid to use the Young–Laplace equation to determine the tension from the shape when $Ca \leqslant 0.1$. This capillary number restriction also holds for expansion. All the contraction runs in figure 17 exhibit tangential flow on the bubble surface pointing from the apex towards the needle tip. The magnitude of the tangential flow is roughly the same as that of the normal velocity. This suggests that the previous models of surfactant transport, which have only considered a normal velocity, should include the contribution of the surface tangential flow as well.

7. Experiment

A series of expansion and contraction experiments was performed to check if the mathematical model captures the physics of bubble motion accurately. The model assumes that the tube is semi-infinite in length with zero wall thickness, that the liquid is unbounded, and that the gas is incompressible. These conditions simplify the numerical simulation, but are not realizable in experiments. Nevertheless, excellent agreement was obtained between the numerical and experimental results, indicating that the assumptions are reasonable.

The apparatus is illustrated in figure 18. An optical system, consisting of a train of pin-hole and lens, forms a collimated light beam of 2.5 cm in diameter from a white light source. The light beam is projected onto the bubble to form a shadow, which is captured by a video camera. The video output is fed into a digitization board (Data Translation, DT2861), installed on a 486 PC. The bubble image is also displayed by a video monitor and saved on a VCR. The gas flow that drives the bubble is controlled by a d.c. motor (Newport, 860A Motorizer, S1058). The direction and speed of the motor are regulated by a power source. Depending on the operating direction, the motor either pushes or draws the plunger of a 1.25 ml syringe, connected via a thin Teflon tube to a three-way miniature solenoid valve (Lee Co.). A computer operates the valve controller and the motor power source. One outlet of the valve leads to an inverted stainless steel needle (Rame-hart, 18 gauge, i.d. 0.7 mm, o.d. 1.2 mm), the other to a run-off. The needle tip where the bubble emerges is submerged in liquid in a rectangular quartz cell ($2.5 \times 4 \times 4.5$ cm). For all the experiments shown below, the contact line appears to be pinned at the inner edge of the needle tip.

The liquid used in this set of experiments was a silicone oil (Dow-Corning, Series 200, 10000 cs fluid). At 22 °C, the viscosity of the silicone oil is (HAAKE Rotovisco RV20 viscometer) 12.0 sPa, the density is (Troemner density meter) 968 kg m^{-3}, and the surface tension is 20.5 mN m^{-1} as measured by a pendant-bubble tensiometer. Air was used to form the bubble.

In a typical run, the syringe, the Teflon tubing, the needle, and the quartz cell are thoroughly cleaned. The d.c. motor is set at a low speed to form a bubble slowly. When

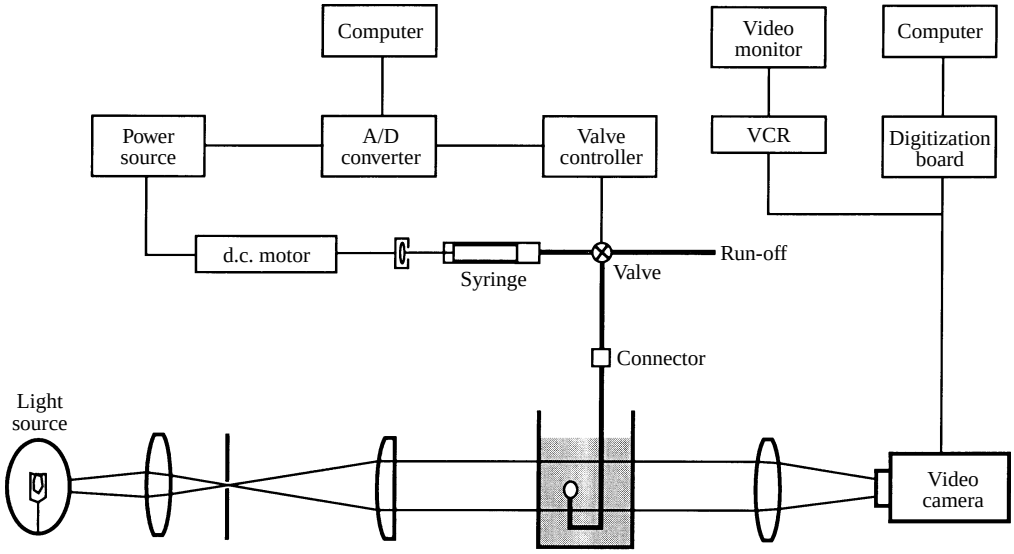

FIGURE 18. Experimental set-up.

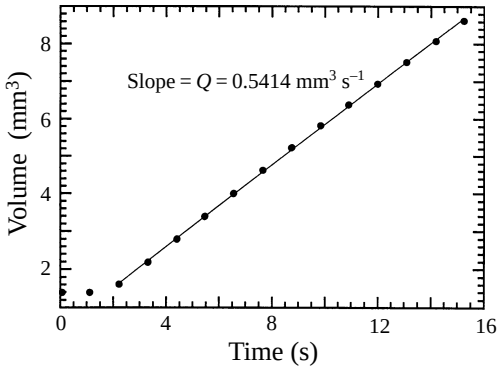

FIGURE 19. A typical plot of the bubble volume as a function of time.

the bubble reaches a desirable size, the valve is turned off, and the bubble relaxes to an equilibrium shape. The speed and direction of the motor are adjusted. The frame grabber is then activated, and immediately the valve is turned on. Fifteen images of the deforming bubble are acquired and digitized by the frame grabber at evenly spaced time intervals. The time interval is chosen so that the total acquisition time is sufficient to capture the complete evolution of the bubble. The digitized images are stored on the digitization board, and are retrieved after the run for edge detection. The edge is located by interpolating the intensity values of two adjacent pixels. This yields bubble shapes with subpixel resolution. The shapes are then saved for further analysis.

To minimize the effect of air compressibility, the syringe and most of the Teflon tubing were filled with water. Only the last section of the delivery line was filled with air. This reduces the total gas volume, so that the change in volume owing to variations in gas pressure is small compared with the bubble volume. Thus, the gas can be treated as incompressible. Figure 19 plots bubble volume versus time for an expansion experiment. The data show that the bubble volume increases linearly with time after the gas flow is turned on at time ≈ 2 s, indicating that air compressibility is not important.

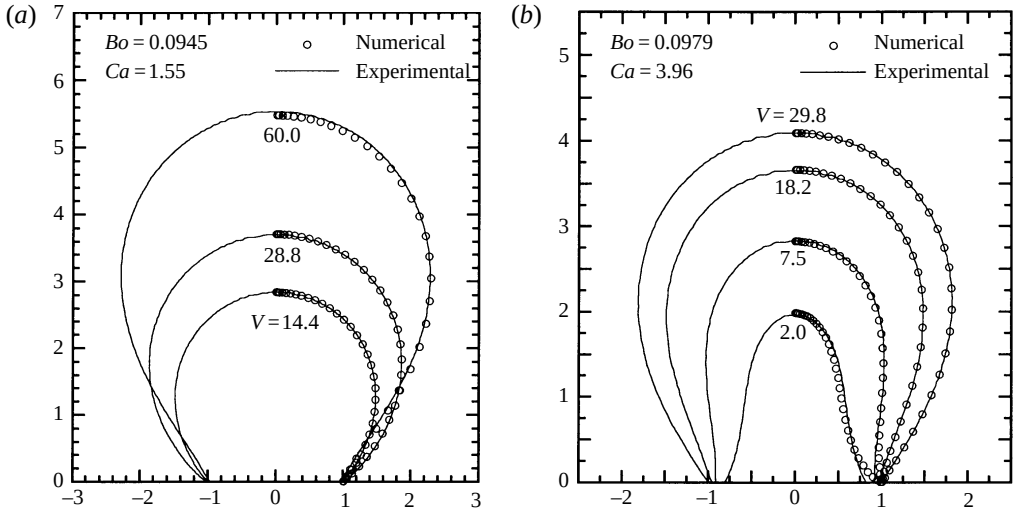

FIGURE 20. Comparison of experimental and numerical results: (*a*) bubble expansion from $V = 14.4$ and (*b*) bubble contraction from $V = 29.8$.

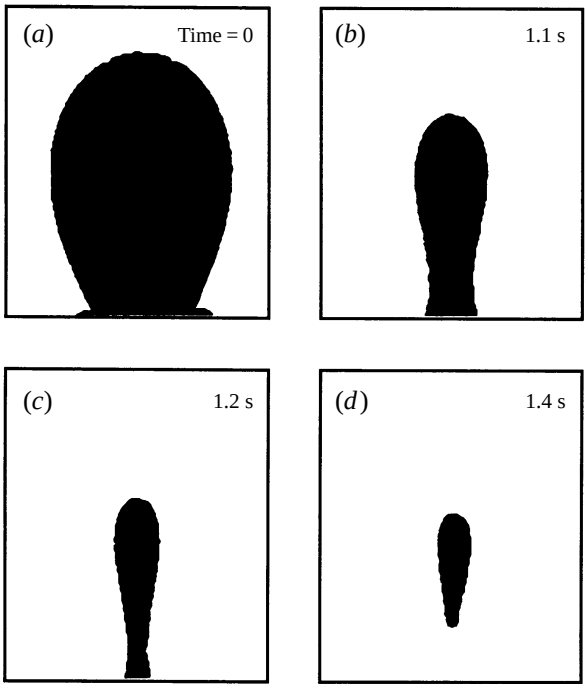

FIGURE 21. A contraction experiment at $Ca = 10$ and $Bo = 0.1$ to illustrate the formation of a satellite bubble.

A linear fit gives the volume flow rate Q, which is used to calculate Ca in the numerical simulation.

Two typical runs are presented in figure 20 as solid lines. Figure 20(*a*) shows bubble expansion from $V = 14.4$ at $Ca = 1.55$ and $Bo = 0.0945$, whereas figure 20(*b*) displays a contraction from $V = 29.8$ at $Ca = 3.96$ and $Bo = 0.0979$. Also plotted in open

circles are the numerical solutions, which are obtained without any adjustable parameter. The excellent agreement confirms the validity of the assumptions made in the mathematical model.

Numerical simulations in §6 have hinted that a contracting bubble may snap off at high Ca. To verify this prediction, a series of contraction experiments was performed and bubble break-up was indeed observed at high Ca. A typical run at $Ca = 10$ is shown in figure 21. It is evident that the contracting bubble breaks up, forming a satellite bubble much smaller than the original static bubble.

8. Conclusions

This work studies the motion of a pinned bubble expanding or contracting from a submerged capillary tip at $Re \ll 1$. Boundary integral solutions of bubble shape, gas pressure, and liquid flow are computed for $0.01 \leqslant Ca \leqslant 100$ and $0.01 \leqslant Bo \leqslant 0.5$. These simulations show that detached bubble volumes approach static values as Ca decreases, and merge into an asymptotic solution at high Ca. Thus, the detached bubble volume is obtained for $0 < Ca < \infty$. The results are useful as a guide for predicting the size of bubbles generated in viscous liquids. These calculations also complement the literature which focuses mainly on inertial effects (Oguz & Prosperetti 1993).

From the bubble expansion results, a correlation has emerged relating the maximum bubble pressure to Ca ((5.11) and figure 12). For small Ca, the maximum pressure occurs when the bubble is hemispherical with radius equal to the tube radius. As Ca increases, the gas pressure peaks at earlier times and the maximum value increases owing to viscous resistance to bubble growth. To measure the dynamic tension, one usually measures the maximum pressure of expanding bubbles at low Ca, since the maximum pressure is simply related to the tension and the tube radius. The correlation derived in this work extends the maximum bubble pressure method to more viscous liquids for which the maximum pressure no longer occurs at the point where the bubble achieves a hemispherical shape.

In the limit $Ca \to 0$, two singular intervals in time have been identified at which the motion of the bubble is dominated by both the viscous and capillary forces. The first is at $t \sim Ca$ during which the step change in gas pressure is balanced mainly by the normal viscous stress. The second is during pinch-off of the neck which is driven by a capillary instability. The rapid contraction of the neck brings the viscous force to the same order as the capillary force. These singularities become apparent in plots of the bubble height as a function of time for different capillary numbers (figures 14, 15 and 16).

Simulations of the contraction of pendant bubbles identify two separate regimes. For $Ca \leqslant 1$, the bubble retracts smoothly back into the tube. However, for larger Ca, the bubble head retracts radially, and the simulations suggest snap-off of a satellite bubble (figure 17).

Experiments on expansion and contraction of pendant bubbles in a silicone oil confirm the validity of the numerical simulations. Experimental loci of bubble shapes are obtained by digitizing video images of the deforming bubble. These experimental loci are in excellent agreement with computed contours. It is observed that a bubble contracting at high Ca snaps off to leave behind a small residue bubble (figure 21).

Appendix A. The Green's functions and local expansions

This Appendix lists the velocity $\hat{\boldsymbol{u}}^{\alpha}$ and stress $\hat{\boldsymbol{T}}^{\alpha}$ at a point $P(r,z)$ generated by a ring force of unit strength located at $\hat{P}(\hat{r},\hat{z})$ and pointing in direction $\boldsymbol{e}_{\alpha}$, $\alpha = r,z$. Define

$$Z = z-\hat{z}, \tag{A 1}$$

$$L = [(r+\hat{r})^2+Z^2]^{1/2}, \tag{A 2}$$

$$D = [(r-\hat{r})^2+Z^2]^{1/2}, \tag{A 3}$$

$$S = [r^2+\hat{r}^2+Z^2]^{1/2}, \tag{A 4}$$

$$m = \frac{2(r\hat{r})^{1/2}}{L}, \tag{A 5}$$

$$K(m) = \int_0^{\pi/2} \frac{\mathrm{d}\theta}{(1-m^2\sin^2\theta)^{1/2}}, \tag{A 6}$$

$$E(m) = \int_0^{\pi/2} (1-m^2\sin^2\theta)^{1/2}\,\mathrm{d}\theta, \tag{A 7}$$

where $K(m)$ and $E(m)$ are the complete elliptic integral of the first and the second kind, respectively. Then,

$$\hat{u}_r^r = \frac{1}{8\pi^2}\frac{1}{r\hat{r}L}\left[K(S^2+Z^2)-E\left(L^2+\frac{Z^2S^2}{D^2}\right)\right], \tag{A 8}$$

$$\hat{u}_z^r = \frac{1}{8\pi^2}\frac{Z}{\hat{r}L}\left[-K+E\frac{S^2-2\hat{r}^2}{D^2}\right], \tag{A 9}$$

$$\hat{u}_r^z = \frac{1}{8\pi^2}\frac{Z}{rL}\left[K-E\frac{S^2-2r^2}{D^2}\right], \tag{A 10}$$

$$\hat{u}_z^z = \frac{1}{4\pi^2}\frac{1}{L}\left[K+E\frac{Z^2}{D^2}\right], \tag{A 11}$$

$$\hat{T}_{rr}^r = \frac{-1}{4\pi^2}\frac{1}{L}\left\{\frac{K}{\hat{r}}\left[\frac{Z^2(S^2-2\hat{r}^2)}{D^2L^2}-\frac{r^2-\hat{r}^2-2Z^2}{r^2}\right]\right.$$
$$\left.+\frac{E}{D^2}\left[\frac{8\hat{r}Z^2(S^2-2r^2)}{D^2L^2}+\frac{r^2(r^2+\hat{r}^2)-S^2(\hat{r}^2+2Z^2)}{r^2\hat{r}}\right]\right\}, \tag{A 12}$$

$$\hat{T}_{rz}^r = \hat{T}_{zr}^r = \frac{-1}{4\pi^2}\frac{Z}{r\hat{r}L}\left\{K\left[\frac{Z^2S^2}{D^2L^2}-2\right]+\frac{E}{D^2}\left[2S^2-Z^2-\frac{16r^2\hat{r}^2Z^2}{D^2L^2}\right]\right\}, \tag{A 13}$$

$$\hat{T}_{zz}^r = \frac{-1}{4\pi^2}\frac{Z^2}{\hat{r}D^2L}\left\{K\frac{2\hat{r}^2-S^2}{L^2}+E\left[1+\frac{8\hat{r}^2(2r^2-S^2)}{D^2L^2}\right]\right\}, \tag{A 14}$$

$$\hat{T}_{rr}^z = \frac{-1}{4\pi^2}\frac{Z}{L}\left\{K\left[\frac{1}{r^2}+\frac{2Z^2}{D^2L^2}\right]+\frac{E}{D^2}\left[6-S^2\left(\frac{1}{r^2}+\frac{8Z^2}{D^2L^2}\right)\right]\right\}, \tag{A 15}$$

$$\hat{T}_{rz}^z = \hat{T}_{zr}^z = \frac{-1}{4\pi^2}\frac{Z^2}{rD^2L}\left\{K\frac{S^2-2r^2}{L^2}-E\left[1+\frac{8\hat{r}^2(2\hat{r}^2-S^2)}{D^2L^2}\right]\right\}, \tag{A 16}$$

$$\hat{T}_{zz}^z = \frac{-1}{2\pi^2}\frac{Z^3}{D^2L^3}\left\{-K+E\frac{4S^2}{D^2}\right\}. \tag{A 17}$$

The local expansions of the Green's functions as $P(r,z)\to\hat{P}(\hat{r},\hat{z})$ are given here. Let the curve on which P and $\hat{P}$ lie have at $\hat{P}$ a tangent circle of radius R and centre O. Then, as $P\to\hat{P}$, we can expand (r,z) in terms of $(\hat{r},\hat{z})$ in a Taylor series:

$$r=\hat{r}+\hat{n}_z\,\Delta s-\frac{\hat{n}_r}{2R}\Delta s^2+\ldots, \tag{A 18}$$

$$z=\hat{z}-\hat{n}_r\,\Delta s-\frac{\hat{n}_z}{2R}\Delta s^2+\ldots, \tag{A 19}$$

where $\hat{\boldsymbol{n}}=\hat{n}_r\,\boldsymbol{e}_r+\hat{n}_z\,\boldsymbol{e}_z$ is a unit vector along $O\hat{P}$, and $\Delta s=s(P)-s(\hat{P})$ is the arclength between P and $\hat{P}$, with the arclength s measured clockwise around O. Then, as $\Delta s\to 0$,

$$\hat{u}_r^r\to\frac{-1}{8\pi^2}\left[\frac{1}{\hat{r}}\ln|\Delta s|-\frac{1}{\hat{r}}(\ln\hat{r}+\ln 8-2-\hat{n}_r^2)\right], \tag{A 20}$$

$$\hat{u}_z^r\to\frac{-1}{8\pi^2}\left[\frac{\hat{n}_r\hat{n}_z}{\hat{r}}\right], \tag{A 21}$$

$$\hat{u}_r^z\to\frac{-1}{8\pi^2}\left[\frac{\hat{n}_r\hat{n}_z}{\hat{r}}\right], \tag{A 22}$$

$$\hat{u}_z^z\to\frac{-1}{8\pi^2}\left[\frac{1}{\hat{r}}\ln|\Delta s|-\frac{1}{\hat{r}}(\ln\hat{r}+\ln 8+\hat{n}_r^2)\right], \tag{A 23}$$

$$\hat{T}_{rr}^r\to\frac{-1}{4\pi^2}\left[\frac{2\hat{n}_z^3}{\hat{r}}\frac{1}{\Delta s}-\frac{3\hat{n}_r\hat{n}_z^2}{\hat{r}R}-\frac{2\hat{n}_z^4-\hat{n}_z^2+3}{2\hat{r}^2}\right], \tag{A 24}$$

$$\hat{T}_{rz}^r\to\frac{-1}{4\pi^2}\left[\frac{-2\hat{n}_r\hat{n}_z^2}{\hat{r}}\frac{1}{\Delta s}+\frac{\hat{n}_z}{\hat{r}}\left(\frac{2\hat{n}_r^2-\hat{n}_z^2}{R}+\frac{\hat{n}_r\hat{n}_z^2}{\hat{r}}\right)\right], \tag{A 25}$$

$$\hat{T}_{zz}^r\to\frac{-1}{4\pi^2}\left[\frac{2\hat{n}_r^2\hat{n}_z}{\hat{r}}\frac{1}{\Delta s}+\frac{\hat{n}_r}{\hat{r}}\left(\frac{2\hat{n}_z^2-\hat{n}_r^2}{R}-\frac{\hat{n}_r(1+2\hat{n}_z^2)}{2\hat{r}}\right)\right], \tag{A 26}$$

$$\hat{T}_{rr}^z\to\frac{-1}{4\pi^2}\left[\frac{-2\hat{n}_r\hat{n}_z^2}{\hat{r}}\frac{1}{\Delta s}+\frac{\hat{n}_z}{\hat{r}}\left(\frac{2\hat{n}_r^2-\hat{n}_z^2}{R}+\frac{\hat{n}_r(\hat{n}_z^2-1)}{\hat{r}}\right)\right], \tag{A 27}$$

$$\hat{T}_{rz}^z\to\frac{-1}{4\pi^2}\left[\frac{2\hat{n}_r^2\hat{n}_z}{\hat{r}}\frac{1}{\Delta s}+\frac{\hat{n}_r}{\hat{r}}\left(\frac{2\hat{n}_z^2-\hat{n}_r^2}{R}+\frac{\hat{n}_r(2\hat{n}_r^2-1)}{2\hat{r}}\right)\right], \tag{A 28}$$

$$\hat{T}_{zz}^z\to\frac{-1}{4\pi^2}\left[\frac{-2\hat{n}_r^3}{\hat{r}}\frac{1}{\Delta s}+\frac{\hat{n}_r^2\hat{n}_z}{\hat{r}}\left(\frac{\hat{n}_r}{\hat{r}}-\frac{3}{R}\right)\right]. \tag{A 29}$$

The next order term in the expansions is at most $O(\Delta s\ln|\Delta s|)$.

Appendix B. Implementation of the Nystrom method

The best way to illustrate the Nystrom method is by an example. Consider the following integral from (4.1 *a*):

$$\int_0^1\frac{T_r(x)\,\hat{u}_r^r(\hat{x};x)}{(1-x)^2}\,\mathrm{d}x=\sum_{i=1}^{N}\frac{T_r(x_i)\,\hat{u}_r^r(\hat{x};x_i)}{(1-x_i)^2}\,w_i, \tag{B 1}$$

where x_i and w_i are the abscissas and weights of the N-point Gauss–Legendre

quadrature. The sum in (B 1) contains N unknowns: $T_r(x_i), i = 1, \ldots, N$. Putting the source point $\hat{x}$ at $x_i, i = 1$ to N, generates N equations. The velocity Green's function $\hat{u}_r^r(\hat{x}; x)$ is singular as $x \to \hat{x}$. An axymptotic analysis yields, as $x \to \hat{x}$,

$$\hat{u}_r^r(\hat{x}; x) = \kappa_0 \ln|x-\hat{x}| + \kappa_1 (x-\hat{x}) \ln|x-\hat{x}| \ldots, \tag{B 2}$$

where κ_0 and κ_1 are independent of x, as shown in Appendix A. The singular part of the integrand in (B 1) is removed by subtraction,

$$\int_0^1 \frac{T_r(x)\,\hat{u}_r^r(\hat{x}; x)}{(1-x)^2}\,\mathrm{d}x = \int_0^1 \left[\frac{T_r(x)\,\hat{u}_r^r(\hat{x}; x)}{(1-x)^2} - \frac{T_r(\hat{x})\,\kappa_0 \ln|x-\hat{x}|}{(1-\hat{x})^2}\right]\mathrm{d}x + \frac{T_r(\hat{x})\,\kappa_0}{(1-\hat{x})^2}\int_0^1 \ln|x-\hat{x}|\,\mathrm{d}x. \tag{B 3}$$

The integrand in the square brackets varies as $(x-\hat{x})\ln|x-\hat{x}|$ as $x \to \hat{x}$, and the Gauss–Legendre quadrature can perform the integration. The Gauss–Legendre quadrature converges exponentially for infinitely differentiable integrands. In the present case, the convergence rate is cubic in N. However, by removing the next highest singular term from the integrand, one can improve the convergence rate systematically.

The integrals in (4.1*b*) with the stress Green's functions are treated similarly. Although the singularity of a stress Green's function is of higher order, no subtraction is needed because the stress Green's functions always appear as a pair and the singular terms cancel between the pair. For example, close to a source point $\hat{s}$,

$$\hat{T}_{rr}^r(\hat{s}; s) \to \frac{\lambda_0}{s-\hat{s}} + \lambda_1 + \ldots, \tag{B 4}$$

where λ_0 and λ_1 are independent of s. Appendix A shows that for a pair of stress Green's functions in (4.1*b*) the leading singular terms multiplied by the appropriate components of the surface normal cancel exactly. Proper cancellation requires that the normal vector be uniquely defined at each point on the surface (i.e. the Lyapunov condition). Thus, the integrands containing the stress Green's functions are well behaved and no subtraction is needed.

We thank the National Science Foundation (PYI grant #CTS-8658147 to D.R.) and the ACS Petroleum Research Fund (#27403-AC9 to D.R. and #29378-AC9 to C.M.) for supporting this work.

REFERENCES

Anderson, D. M. & Davis, S. H. 1993 Two-fluid viscous flow in a corner. *J. Fluid Mech.* **257**, 1–31.

Bhavaraju, S. M., Russell, T. W. F. & Blanch, H. W. 1978 The design of gas sparged devices for viscous liquid systems. *AIChE J.* **24**, 454–466.

Chandrasekhar, S. 1961 *Hydrodynamic and Hydromagnetic Stability*. Clarendon.

Clift, R., Grace, J. R. & Weber, M. E. 1978 *Bubbles, Drops, and Particles*. Academic.

Datta, R. L., Napier, D. H. & Newitt, D. M. 1950 The properties and behaviour of gas bubbles formed at a circular orifice. *Trans. Instn Chem. Engrs* **28**, 14–26.

Davidson, J. F. & Schuler, B. O. G. 1960*a* Bubble formation at an orifice in a viscous liquid. *Trans. Instn Chem. Engrs* **38**, 144–154.

Davidson, J. F. & Schuler, B. O. G. 1960*b* Bubble formation at an orifice in an inviscid liquid. *Trans. Instn Chem. Engrs* **38**, 335–342.

Delves, L. M. & Mohamed, J. L. 1985 *Computational Methods for Integral Equations*. Cambridge University Press.

Edwards, D. A., Brenner, H. & Wasan, D. T. 1991 *Interfacial Transport Processes and Rheology*. Boston. Butterworth–Heinemann Series in Chemical Engineering.

Joos, P. & Rillaerts, E. 1981 Theory on the determination of the dynamic surface tension with the drop volume and maximum bubble pressure methods. *J. Colloid Interface Sci.* **79**, 96–100.

Khurana, A. K. & Kumar, R. 1969 Studies in bubble formation-iii. *Chem. Engng Sci.* **24**, 1711–1723.

Kumar, R. & Kuloor, N. R. 1970 The formation of bubbles and drops. *Adv. Chem. Engng* **8**, 255–368.

Kupferberg, A. & Jameson, G. J. 1969 Bubble formation at a submerged orifice above a gas chamber of finite volume. *Trans. Instn Chem. Engrs* **47**, T241–T250.

Ladyzhenskaya, O. A. 1969 *The Mathematical Theory of Viscous Incompressible Flow*. Gordon & Breach.

LaNauze, R. D. & Harris, I. J. 1972 On a model for the formation of gas bubbles at a single submerged orifice under constant pressure conditions. *Chem. Engng Sci.* **27**, 2102–2105.

LaNauze, R. D. & Harris, I. J. 1974 Gas bubble formation at elevated system pressures. *Trans. Instn Chem. Engrs* **52**, 337–347.

Liow, J. L. & Gray, N. B. 1988 A model of bubble growth in wetting and non-wetting liquids. *Chem. Engng Sci.* **43**, 3129–3139.

Longuet-Higgins, M. S., Kerman, B. R. & Lunde, K. 1991 The release of air bubbles from an underwater nozzle. *J. Fluid Mech.* **230**, 365–390.

MacLeod, C. A. & Radke, C. J. 1994 Surfactant exchange kinetics at the air/water interface from the dynamic tension of growing liquid drops. *J. Colloid Interface Sci.* **166**, 73–88.

Marmur, A. & Rubin, E. 1976 A theoretical model for bubble formation at an orifice submerged in an inviscid liquid. *Chem. Engng Sci.* **31**, 453–463.

Michael, D. H. 1981 Meniscus stability. *Ann. Rev. Fluid Mech.* **13**, 189–215.

Miller, R., Joos, P. & Fainerman, V. B. 1994 Dynamic surface and interfacial tensions of surfactant and polymer solutions. *Adv. Colloid Interface Sci.* **49**, 249–302.

Miller, R., Policova, Z., Sedev, R. & Neumann, A. W. 1993*a* Relaxation behavior of human albumin adsorbed at the solution/air interface. *Colloids and Surfaces* **76**, 179–185.

Miller, R., Sedev, R., Schano, K. H., Ng, C. & Neumann, A. W. 1993*b* Relaxation of adsorption layers at solution/air interfaces using axisymmetric drop-shape analysis. *Colloids Surfaces* **69**, 209–216.

Moffatt, H. K. 1964 Viscous and resistive eddies near a sharp corner. *J. Fluid Mech.* **18**, 1–18.

Oguz, H. N. & Prosperetti, A. 1993 Dynamics of bubble growth and detachment from a needle. *J. Fluid Mech.* **257**, 111–145.

Pan, R., Green, J. & Maldarelli, C. 1995 *J. Colloid Interface Sci.* (submitted).

Pozrikidis, C. 1992 *Boundary Integral and Singularity Methods for Linearized Viscous Flow*. Cambridge University Press.

Prosperetti, A., Oguz, H. N. & Won, K. J. 1997 Formation and rise of large gas bubbles in very viscous fluids. *PPG Tech. J.* **3**, 97–114.

Rallison, J. M. & Acrivos, A. 1978 A numerical study of the deformation and burst of a viscous drop in an extensional flow. *J. Fluid Mech.* **89**, 191–200.

Ramakrishnan, S., Kumar, R. & Kuloor, N. R. 1969 Studies in bubble formation-I: bubble formation under constant flow conditions. *Chem. Engng Sci.* **24**, 731–747.

Salamon, T. R., Bornside, D. E., Armstrong, R. C. & Brown, R. A. 1995 The role of surface tension in the dominant balance in the die swell singularity. *Phys. Fluids* **7**, 2328–2344.

Satyanarayan, A., Kumar, R. & Kuloor, N. R. 1969 Studies in bubble formation-II: bubble formation under constant pressure conditions. *Chem. Engng Sci.* **24**, 749–761.

Schultz, W. W. & Gervasio, C. 1990 A study of the singularity in the die-swell problem. *Q. J. Appl. Maths* **43**, 407–425.

Tan, R. B. H. & Harris, I. J. 1986 A model for non-spherical bubble growth at a single orifice. *Chem. Engng Sci.* **41**, 3175–3182.

Tanveer, S. & Vasconcelos, G. L. 1995 Time-evolving bubbles in two-dimensional Stokes flow. *J. Fluid Mech.* **301**, 325–344.

Tritton, D. J. & Egdell, C. 1993 Chaotic bubbling. *Phys. Fluids* A **5**, 503–505.

Tsuge, H. & Hibino, S. I. 1983 Bubble formation from an orifice submerged in liquids. *Chem. Engng Commun.* **22**, 63–79.

Van Krevelen, D. W. & Hoftijzer, P. J. 1950 Studies of gas-bubble formation: calculation of interfacial area in bubble contactors. *Chem. Engng Progr.* **46**, 29–35.

Walters, J. K. & Davidson, J. F. 1963 The initial motion of a gas bubble formed in an inviscid liquid. *J. Fluid Mech.* **17**, 321–340.

Wraith, A. E. 1971 Two stage bubble growth at a submerged plate orifice. *Chem. Engng Sci.* **26**, 1659–1671.